Multi-resolution open-top light-sheet microscopy to enable 3D pathology of lymph nodes for breast cancer staging

Lindsey A. Barner

A dissertation

submitted in partial fulfillment of the

requirements for the degree of

Doctor of Philosophy

University of Washington

2022

Reading Committee:

Jonathan T.C. Liu, Chair

Ramkumar Sabesan

Suzanne M. Dintzis

Nathan J. Sniadecki

Program Authorized to Offer Degree:

Mechanical Engineering

University of Washington

Abstract

Multi-resolution open-top light-sheet microscopy to enable
3D pathology of lymph nodes for breast cancer staging

Lindsey A. Barner

Chair of the Reading Committee:
Professor Jonathan T.C. Liu
Mechanical Engineering

Slide-based histopathology is the clinical gold-standard technique used to diagnose cancer and determine a patient's prognosis. Unfortunately, its basis in sparse 2D visualization and tedious, destructive tissue processing reduces diagnostic accuracy, reproducibility, and inter-observer agreement, potentially compromising the quality of patient treatment. To address these limitations, open-top light-sheet microscopy (OTLS) has been developed for rapid, nondestructive 3D imaging of large pathology specimens. It offers the same level of detail as traditional pathology slides and has been applied to various pathology applications such as breast and prostate cancer. In this work, we overcome several limitations of previous OTLS architectures such as limited imaging depth and an inability to accommodate various clearing protocols with development of a solid immersion meniscus lens (SIMlens). A SIMlens is a wavefront-matching element that enables the use of air-based objectives, which, when implemented with a turret in OTLS microscopy, allows users to rapidly transition between low- and high-resolution 3D views. We report development of the first multi-resolution OTLS microscope based on this SIMlens technology, which enables efficient 3D imaging in diagnostic pathology applications. Additionally, we explore how multi-resolution

OTLS microscopy may facilitate improved management of breast cancer patients. We showcase a comprehensive 3D pathology workflow for staging metastases in whole lymph nodes with multi-resolution OTLS microscopy, and demonstrate that this workflow may improve breast cancer staging accuracy in comparison to standard of care.

Finally, to further streamline diagnosis with 3D pathology, we implement a deep learning-based computational triage method to automatically segment suspicious regions in 3D pathology datasets to guide pathologist review. We demonstrate this method with screening and diagnosis of dysplasia and esophageal adenocarcinoma (EAC) in endoscopic biopsies from patients with Barrett's esophagus (a precursor to EAC). In future work we aim to show that our AI-assisted 3D pathology method may improve diagnostic sensitivity of neoplasia in endoscopic biopsies while reducing the amount of information that pathologists must review. Importantly, this could facilitate earlier detection and treatment of EAC.

TABLE OF CONTENTS

LIST OF FIGURES

Chapter 1. INTRODUCTION

1.1 CLINICAL PROBLEM

Histopathology is the gold-standard technique for diagnosing a vast range of diseases and malignancies such as breast, lung, and prostate cancer (the most commonly diagnosed cancers in the United States) [1]. Unfortunately, histopathology has a number of limitations. It is time- and labor-intensive, requiring several days for formalin fixation, paraffin embedding, sectioning, mounting onto slides, and hematoxylin and eosin (H&E) staining [2]. It is destructive to the tissue, preventing the use of downstream diagnostic tools such as DNA sequencing and molecular assays. Additionally, only a few thin sections (~ 5 μm thickness) of the specimen are submitted for pathologic analysis, making the technique prone to sampling errors. Finally, histopathology only provides pathologists with a two-dimensional (2D) view of the tissue specimen, which makes it difficult to visualize important pathologic structures in their native three-dimensional (3D) context.

Among others, these factors contribute to the high rates of inter- and intra- observer variability that have hindered slide-based histology for years. This reduces the prognostic power of the technique and complicates treatment decisions. For example, inter-observer variability in pathologic grading of core-needle biopsies for prostate cancer complicates stratification of patients who may benefit from active surveillance instead of curative therapies such as surgery [3], [4]. Prognosis and treatment plans are heavily influenced by the pathologic grade of an individual's core-needle biopsy; patients with Gleason scores of 6 or lower are typically recommended for active surveillance, whereas Gleason scores of 7 and higher are often recommended for curative therapies [5]. With inter-observer agreement as low as $\kappa = 0.35$ (Cohen's kappa) in some cases, ambiguity can cause under- or over-treatment of certain patients, resulting in increased morbidity

and mortality (in the case of under-treatment of aggressive disease) or unnecessary side effects such as incontinence and impotence (in the case of over-treatment of indolent disease) [3], [6].

1.2 LIGHT-SHEET FLUORESCENCE MICROSCOPY (LSFM)

Over the years, a host of imaging techniques have shown the potential to serve as alternatives to slide-based histology and overcome the limitations discussed previously. These include microscopy with ultraviolet surface excitation (MUSE) [7], stimulated Raman spectroscopy (SRS) [8], optical coherence tomography (OCT) [9], photoacoustic microscopy (PAM) [10], confocal microscopy [11], and light-sheet fluorescence microscopy (LSFM) [12], among others.

Light-sheet fluorescence microscopy (LSFM) shows particular promise as an alternative to slide-based histology due to its ability to rapidly image in 3D with nondestructive optical sectioning (Figure 1.1). LSFM has rapidly risen in popularity as a tool for three-dimensional (3D) and time-lapse (4D) imaging of biological specimens. LSFM combines optically efficient planar illumination (hence the term light "sheet" microscopy) with fast camera-based acquisition that detects fluorescence orthogonal to the direction of illumination [13], [14]. LSFM yields unprecedented imaging speeds (with minimal photobleaching and phototoxicity) compared to point- or line-scanned techniques, such as confocal microscopy, SRS, and PAM. Compared to surface-based imaging approaches such as MUSE, which penetrates just a few microns into tissue, LSFM enables imaging several millimeters deep in optically cleared specimens.

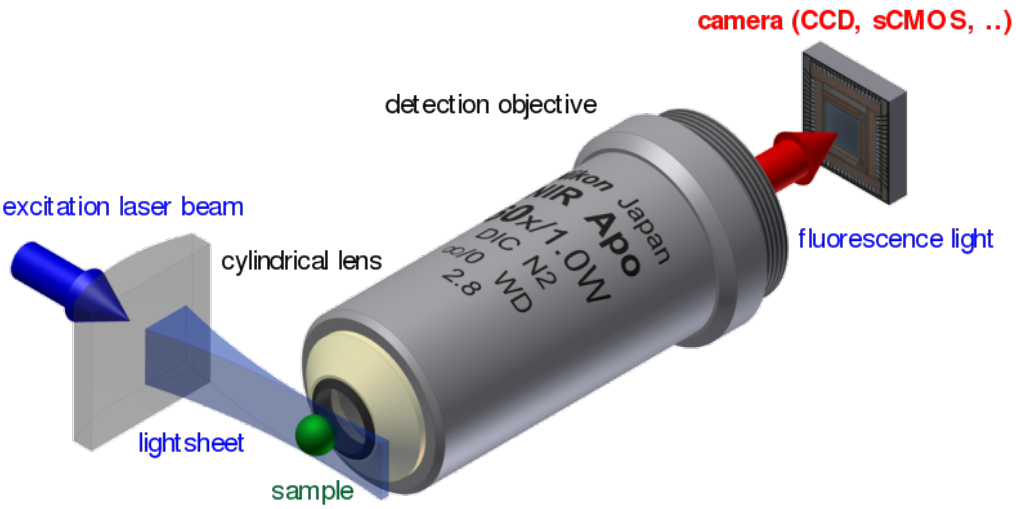

Figure 1.1. Diagram of a light-sheet fluorescence microscopy (LSFM) setup. The illumination beam is focused to a planar sheet ("light sheet") in the specimen. An objective positioned orthogonally to the light sheet relays generated fluorescence to a high-speed camera. Volumetric images are generated by translating the specimen through the light sheet or by optically scanning the optical beams through the specimen. Figure obtained from Wikipedia.

1.3 Motivation for open-top light-sheet microscopy (OTLS)

Early LSFM microscopy systems, also known as selective plane illumination microscopy (SPIM), were used for imaging small model organisms in which samples were typically embedded in agarose and placed within cuvettes or capillary tubes [15], [16]. Variants such as ultramicroscopy and inverted selective plane illumination microscopy (iSPIM) later emerged for applications involving larger specimens, but still imposed geometric constraints due to bulky objectives being positioned to the side or above the samples (Figure 1.2) [17], [18].

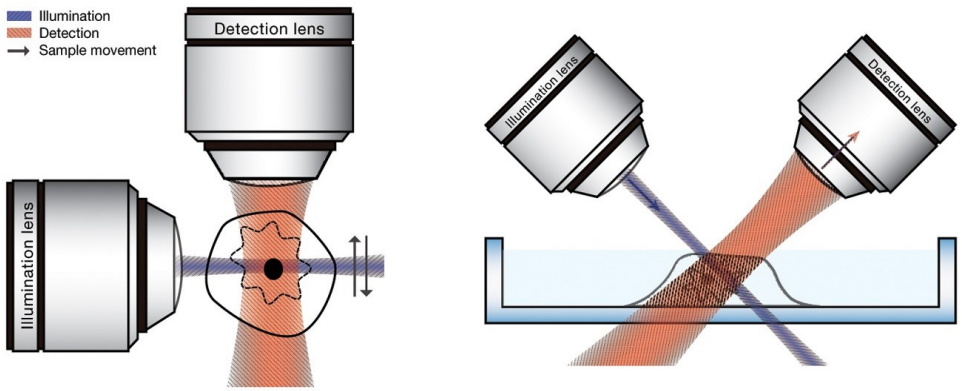

Figure 1.2. (Left) Optical architecture for a conventional horizontal SPIM arrangement (ultramicroscope, for example) as opposed to (right) a tilted architecture such as iSPIM. In both architectures, objective positions impose geometric constraints on specimen size. Figure adapted from [13].

To address some of these sample-mounting and size limitations [19]–[22], we and others have developed open-top light-sheet (OTLS) microscopes as versatile, easy-to-use platforms for imaging cleared tissues of arbitrary size and number [23]–[28]. In OTLS microscopy, cleared specimens are simply placed on a flat, transparent sample holder and imaged from below, similar to how a document is placed and imaged on a flatbed scanner (Figure 1.3). All optical components are located below the sample holder, leaving the physical space above the holder unconstrained. This enables specimens of nearly any size or shape to be mounted for imaging [29]. During imaging, the sample and sample plate are stage-scanned through the stationary light sheet in three dimensions (XYZ) to create a volumetric image of the specimen.

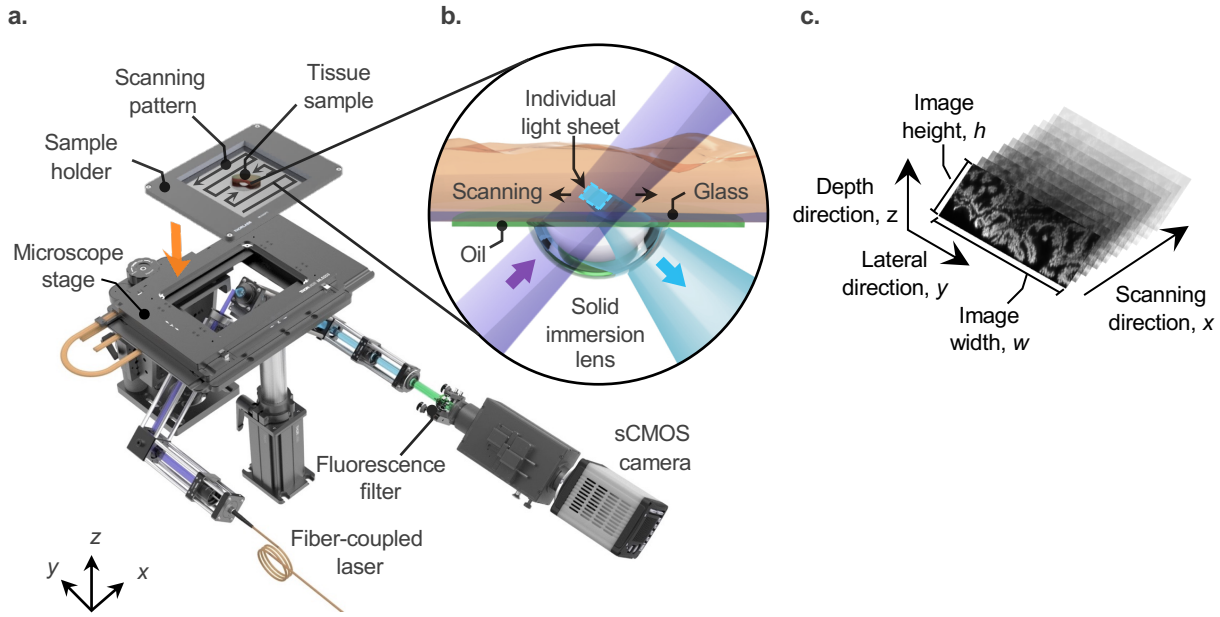

Figure 1.3. (a) Our first demonstration of OTLS microscopy. Samples of any size, shape, or quantity may be placed on the sample holder for imaging. The holder is translated through the light sheet by the microscope stage during imaging. (b) This architecture utilized a solid immersion lens (SIL) as a wavefront-matching element to prevent aberrations that would otherwise occur with a flat interface. The center of curvature of the SIL is coincident with the focal point of the illumination and collection beams (purple and blue, respectively). Therefore the surface of the SIL is approximately perpendicular to the optical rays, so they may transition across the glass interface without inducing aberrations. (c) As the sample is translated through the light sheet in the scanning direction, oblique 2D images are captured in succession to create a 3D volumetric image. Figure adapted from [23].

One of the challenges unique to OTLS microscopy is that the illumination and collection beams are angled relative to the flat sample plate (45 degrees). This can introduce significant aberrations. Our first demonstration of OTLS [23] suppressed these aberrations by employing a hemispherical solid immersion lens (SIL) below the sample plate, as shown in Figure 1.3. [30]. The SIL has a curved outer surface for which the center of curvature is coincident with the foci of the illumination and collection beams. In other words, the SIL's outer surface matches the

wavefront curvature of the illumination and collection beams, minimizing aberrations as the beams transition between air and glass. A thin layer of index-matching oil spans the small gap between the top surface of the stationary SIL and the translating sample plate, enabling the plate to move smoothly during imaging. It should be noted that the SIL increases the numerical aperture (NA) of the beams by a factor of the SIL's refractive index, n (which should be exactly matched to that of the sample plate, oil layer, and sample). This is because $\mathrm{NA} = n \times \sin(\theta)$, where the ray angles ($\theta$) are unchanged as they transition between air and the higher-index SIL material.

The clinical utility of 3D imaging was demonstrated with volumetric microscopy of prostate biopsies and grading of prostate cancer with this OTLS system [23]. Human biopsy specimens (~ 2 cm in length, 1 mm in diameter) were stained with an H&E fluorescent analog stain (nuclear and cytoplasmic stains), optically cleared, and then imaged with OTLS microscopy. Images were post-processed with a Beer-Lambert based algorithm to mimic the color palette of H&E histology (Figure 1.4) [31], [32].

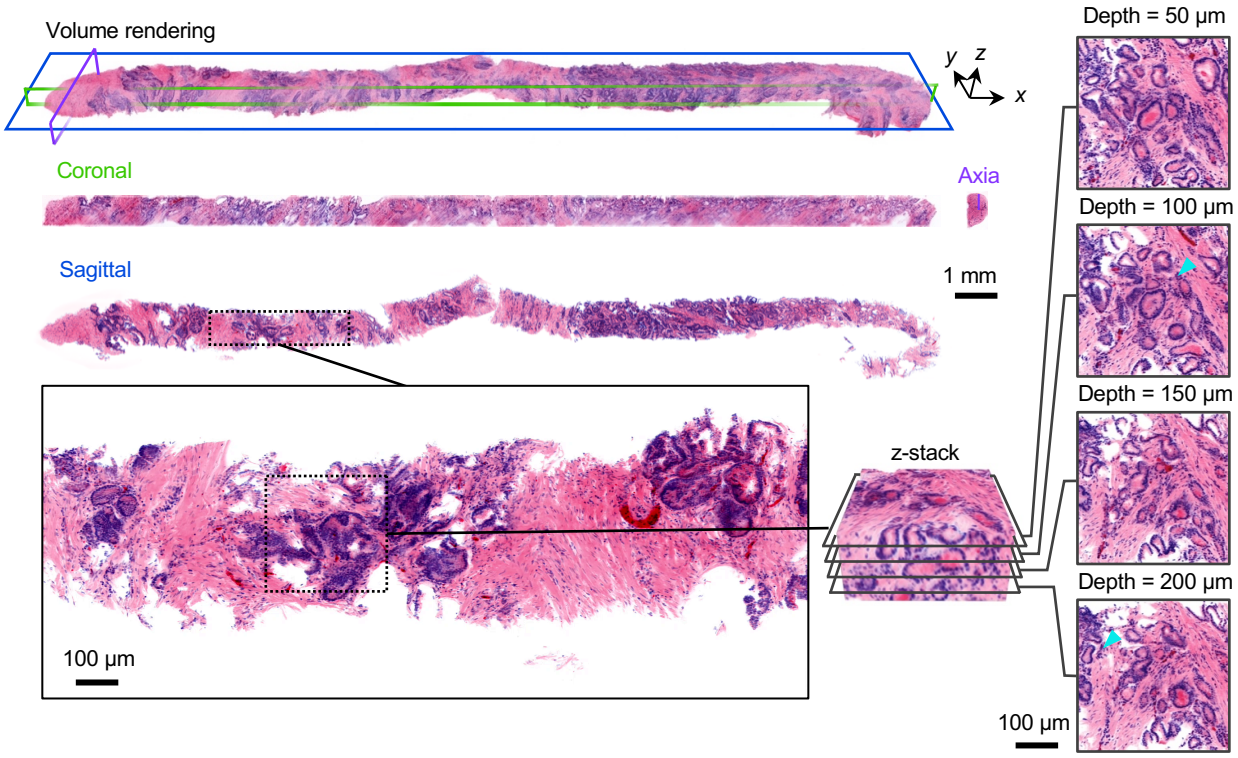

Figure 1.4. Volumetric microscopy of a core-needle prostate biopsy, imaged with our first SIL-based OTLS architecture. Biopsies were stained with an H&E fluorescent analog stain (DRAQ5 and eosin), optically cleared with CLARITY-X, and imaged with OTLS in two channels. The images were post-processed with a Beer-Lambert coloring algorithm to give the images a conventional H&E-like appearance. Figure adapted from [23].

Chapter 2. DEVELOPMENT OF A SOLID IMMERSION MENISCUS LENS (SIMLENS)

2.1 MOTIVATION FOR A SOLID IMMERSION MENISCUS LENS (SIMLENS)

The development of open-top light-sheet (OTLS) microscopy in prior work has expanded the scope of LSFM to imaging specimens of almost any size, shape, or quantity [23], [25], [27], [28]. This has given OTLS the potential to resolve many limitations of slide-based histology. Pathology specimens may be rapidly imaged in 3D, overcoming sampling errors associated with histology and enabling pathologists to view specimens in a volumetric context. Additionally, OTLS reduces the required sample preparation to hours rather than days as is required for histology. Finally, sample preparation and imaging are nondestructive to the specimen, enabling downstream molecular assays if desired.

In OTLS microscopy, the illumination and collection axes are oriented at 45° angles with respect to the vertical axis below the sample holder. This geometry requires careful refractive index and/or wavefront matching to suppress aberrations as the beams transition across oblique interfaces with different refractive indices (e.g. sample holder, specimen, air, etc.). As was previously discussed, early implementations of OTLS used a solid immersion lens (SIL) to provide an approximately normal interface for the focusing beams as they transition between air and a higher-index medium (Figure 2.1). Although a SIL conveniently suppresses aberrations in OTLS microscopy, it has several limitations. In a SIL-based OTLS architecture, vertical motion of the sample is limited because the SIL's flat upper surface must be positioned closely to the sample plate, with a thin layer of index-matching oil spanning the gap. Thus, 3D scanning is restricted to the proximity of the sample's surface. Additionally, SIL-based OTLS microscopes cannot

accommodate a variety of clearing protocols, as the refractive index of the sample, sample plate, and oil layer must closely match that of the SIL [23]–[25].

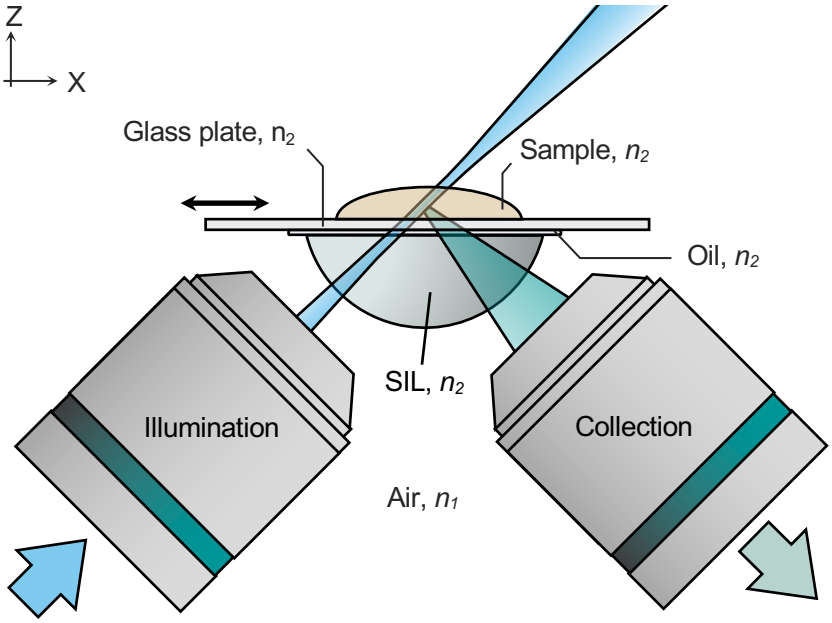

Figure 2.1. Our first demonstration of OTLS microscopy employed a solid immersion lens (SIL) to suppress aberrations induced by the oblique angle of the illumination and collection beams relative to the sample plate. The SIL is positioned beneath the glass sample plate and has a curved outer surface which is perpendicular to the optical rays. This prevents aberrations as the optical rays transition between the air and glass interface, as would otherwise occur at a flat interface. However, vertical motion of the sample is limited because the top surface of the stationary SIL must remain in close proximity to the sample plate.

Alternatively, a more-recent implementation of OTLS employs a multi-immersion collection objective dipped within an immersion chamber, which enables vertical motion of the sample up to several millimeters [27]. However, immersion objectives are significantly more expensive than air-based objectives and are not as readily available at a variety of magnifications, NAs, and fields of view. Additionally, immersion objectives cannot be easily changed without first

emptying the liquid in the immersion chamber, making it logistically difficult to switch between objectives (if so desired).

2.2 A SIMLENS FOR OTLS MICROSCOPY

To overcome the limitations of a SIL, we have developed a solid immersion meniscus lens (SIMlens) for OTLS microscopy as shown in Figure 2.2 [33]. A SIMlens offers a number of advantages in context of OTLS:

(1) A SIMlens enables movement of the sample and sample plate in all three dimensions. In the design shown in Figure 2.2a, a SIMlens seals an immersion chamber and is placed in front of a standard air objective. Both surfaces of the SIMlens share a common center of curvature, which is aligned to the focal point of the air objective. Similar to the case of a SIL, the curved surfaces prevent refractive aberrations and provide an increase in NA and magnification. However, in contrast to a SIL-based OTLS architecture, the sample plate for a SIMlens-based OTLS design is located on top of a liquid reservoir rather than above the flat surface of a SIL (Figure 2.2b). This frees the sample and sample plate to move vertically (in z), albeit limited by the working distance of the objective in a 45° geometry. Thus, 3D imaging may be performed several millimeters deep into tissue (Figure 2.2b).

(2) The SIMlens accommodates samples prepared with a wide variety of clearing protocols (n = 1.33 – 1.56). Similar to a SIL-based OTLS microscope, the refractive index of the sample, sample plate, and immersion medium must ideally be matched, as described in a recent report that explores various sample holder materials for effective index matching [27]. However, unlike a SIL-based OTLS microscope, the index of the SIMlens does not need to be matched to that of the sample – since both surfaces of the SIMlens perform wavefront matching, index matching is not needed.

(3) When compared to OTLS systems that utilize immersion objectives dipped in an index-matching bath [27], [28], a SIMlens enables the use of less-expensive air objectives that are readily available at various magnifications, NAs, and fields of view. Additionally, a SIMlens may enable rapid multi-resolution OTLS imaging (e.g. with a turret of air objectives). This is in contrast to OTLS systems that utilizes immersion objectives [27], as the objectives cannot be easily changed without first emptying the liquid in the immersion chamber, making it logistically difficult to switch between objectives (if so desired). Unlike previous OTLS systems that use flat prisms in front of air-based objectives to mitigate off-axis aberrations [25], a SIMlens increases NA and additionally provides wavefront matching for superior aberration mitigation.

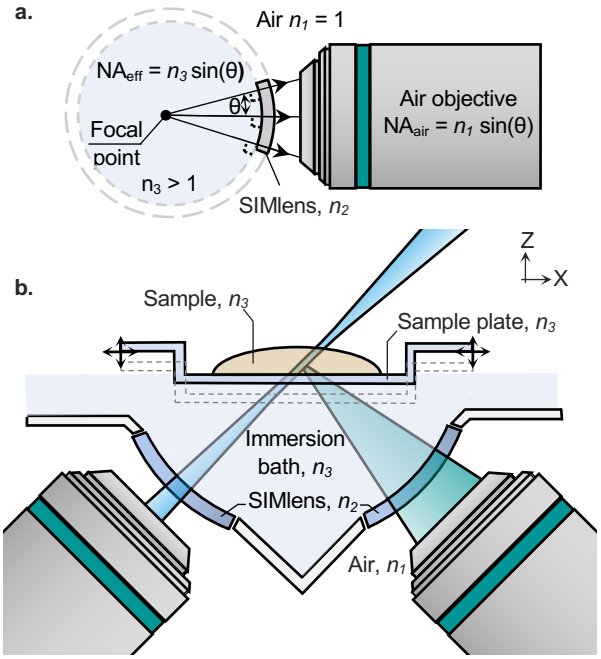

Figure 2.2. (a) A SIMlens positioned in front of an air objective. Both SIMlens surfaces have a radius of curvature that is coincident with the objective's focal point, so that rays emanating from the focal point do not refract as they cross both SIMlens surfaces. Since ray angles are preserved (θ), NA and magnification increase by a factor of n_3, the refractive index of the immersion medium. (b) A SIMlens paired with an air-based objective in OTLS microscopy suppresses off-axis and

spherical aberrations. This architecture accommodates a variety of immersion media and enables a rapid exchange of objectives for multi-resolution imaging. Figured adapted from [34].

2.3 VALIDATION OF SIMLENS PERFORMANCE

2.3.1 *USAF*

To validate the performance of a SIMlens, we first show with a simple back-illuminated imaging setup (Figure 2.3a) that a SIMlens is compatible with a wide range of immersion media (n = 1.00 - 1.56). The imaging performance of this setup approximates that of an OTLS collection arm under the assumption that ideal index matching is achieved between the sample plate and immersion media (Figure 2.3b). Similar to a SIL, a SIMlens improves the resolution (i.e. boosts NA) and increases magnification of an air objective by a factor of the immersion medium's refractive index. We imaged a negative-transmission USAF resolution target immersed in various media (n = 1.00, air; n = 1.33, water; and n = 1.56, ethyl cinnamate) with long-working-distance air objectives (WD ≈ 20 mm) and a custom-fabricated SIMlens (five custom SIMlenses were obtained from BMV Optical Technologies Inc. for $700 each). The target was back-illuminated with an LED at $\lambda \approx 450$ nm and images were acquired with a 10X (NA_{air} = 0.21, MUL04101) or a 20X (NA_{air} = 0.40, MUE21200) objective, as shown in Figure 2.4.

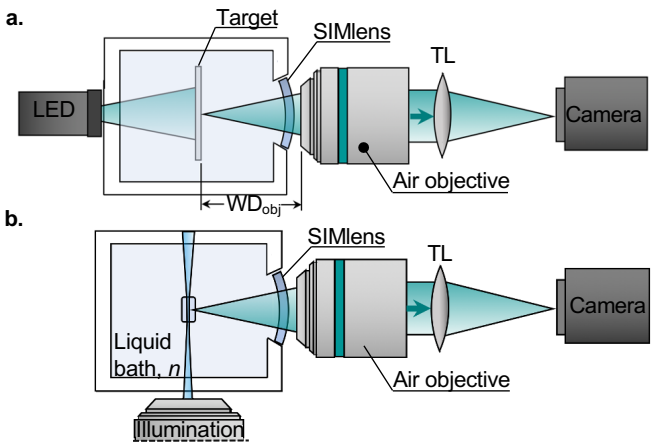

Figure 2.3. (a) The optical setup used to demonstrate that a SIMlens is compatible with various immersion media. A resolution target (USAF) is back-illuminated in an air or liquid medium (n = 1.00, 1.33, or 1.56). The detection arm consists of a SIMlens, air objective (10X or 20X), tube lens, and camera. (b) The optical setup used to demonstrate resolution uniformity when using a SIMlens on the detection arm of a light-sheet microscope. A light sheet illuminates a sample immersed in a liquid bath (of refractive index n). Fluorescence signal is imaged onto a camera with the same SIMlens-based setup used in (a). Figure adapted from [34].

From the images, we measured the edge response at the center of the FOV, from which, as described in [35], the Fourier transform of the first derivative was used to estimate the modulation transfer function (MTF). Assuming uniform illumination through a circular collection aperture, the MTF's limiting resolution at a 9% modulation depth approximates resolution according to the Rayleigh criterion [36]. According to these assumptions, the measured resolution was found to be within 30% of the diffraction limit (Rayleigh criterion), and scales inversely with the index of the immersion medium. Experimental results (Figure 2.4c) confirm that this relationship is valid over a range of refractive indices corresponding to standard clearing protocols.

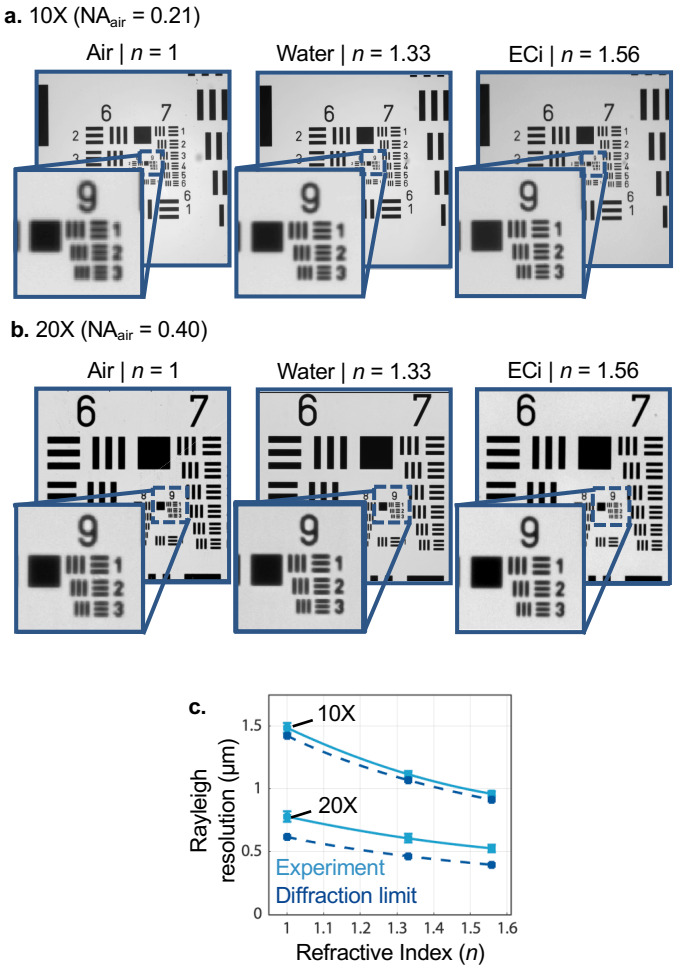

Figure 2.4. Images of a resolution target in media of different refractive indices. Images were obtained with a (a) 10X air objective or (b) 20X air objective. Although magnification increases with n, images are cropped to the same field of view. (c) As anticipated, resolution (according to Rayleigh criterion) measured at the center of the field of view improves as n increases (resolution $\propto 1/n$) and is measured to be within 10% and 30% of the diffraction limit when using a 10X and 20X objective, respectively. Figure adapted from [34].

2.3.2 *PSFs*

Second, we show with a conventional LSFM setup (Figure 2.3b) that imaging resolution with a SIMlens is uniform to within 10% across the imaged FOV. This simple setup allowed us to assess the feasibility of the SIMlens concept prior to developing a full SIMlens-based OTLS system. It approximates the performance of an OTLS imaging setup under the assumption that ideal index

matching is achieved between the sample, sample holder, and immersion medium. Note that SIMlens performance was only tested on the higher-NA collection side; a SIMlens will not aberrate the illumination sheet if a low NA of less than 0.1 is used (Zemax simulations, data not shown). Agarose phantoms (1% w/v) containing a uniform distribution of 175-nm diameter gold nanoparticles (sub-diffraction-limited) were prepared and imaged in reflectance in a high-index medium (n = 1.56; ethyl cinnamate).

The width of the illumination light sheet (1 mm) filled one dimension of the camera's FOV. In the other dimension, the light sheet (depth of focus ≈ 120 μm) was tiled axially across the image plane [37]. We imaged the phantoms with both 10X and 20X air objectives (setup shown in Figure 2.3b). We quantified the lateral resolution across the FOV by measuring the full-width-at-half-maximum (FWHM) of a Gaussian fit to the detected PSFs. For both objectives, the resolution at the edges of the FOV were < 10% degraded in comparison to the center of the FOV (Figure 2.5). Note that degradation in resolution at the edges of the FOV will increase as an objective's NA increases, and as the radius of curvature of a SIMlens decreases. These two issues are coupled since the working distance of objectives typically decreases as NA increases. Thus, aberrations at the edges of the FOV may become unacceptable for applications requiring a higher NA than what was explored here (NA_{air} = 0.40).

Zemax simulations confirm the results shown in Figure 2.5. After modeling the optical path consisting of a SIMlens, air objective (10X and 20X, US patents 8,958,154 B2 and 7,848,027 B2), and tube lens, we plotted the FWHM of simulated PSFs (Huygens PSF) for field points across the FOV. As with the experimental measurements, the simulated PSFs exhibited < 10% degradation across the FOV and matched the experimental results to within 20% (Figure 2.5).

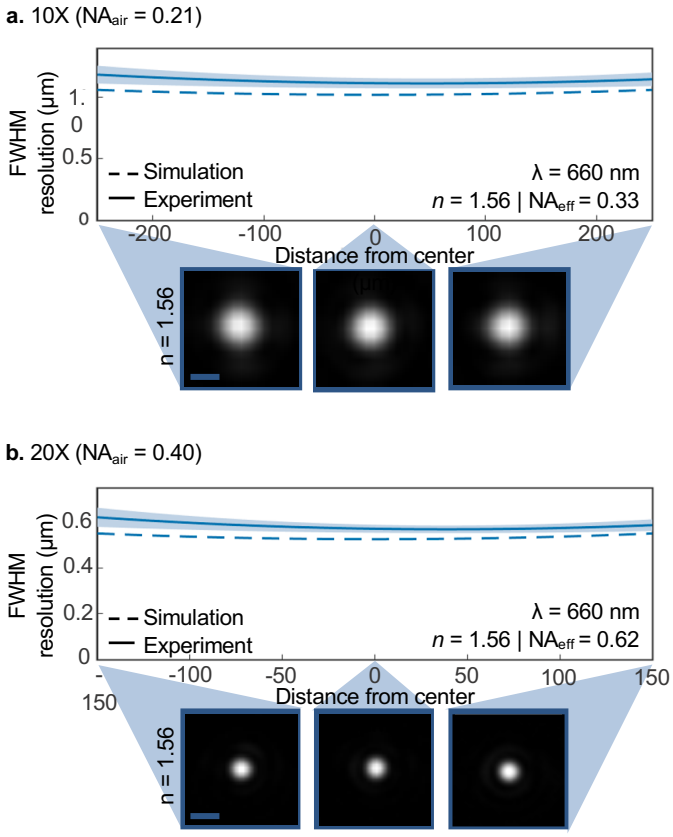

Figure 2.5. Images of sub-diffraction beads in $n = 1.56$ (ECi) were obtained to assess resolution at various points across the field of view. (a) The measured lateral resolution (FWHM of main lobe) across the FOV is plotted for a 10X objective. The use of a SIMlens with an immersion medium at $n = 1.56$ results in an effective NA (NA_{eff}) of 0.33. Measurement uncertainty (standard deviation) is indicated by the shaded region. Also shown are theoretical results based on Zemax simulations. Representative bead images are shown as acquired from the left, center, and right edges of the FOV. (b) Similar results are shown for a 20X air objective ($NA_{eff} = 0.62$). Scale bars are 5 μm. Figure adapted from [34].

2.4 SIMLENS-BASED MULTI-RESOLUTION LSFM IMAGING OF HUMAN PROSTATE TISSUE

We performed multi-resolution LSFM imaging in an optically cleared human tissue specimen. By utilizing a SIMlens, convenient multi-resolution imaging (for low to moderate NAs as

demonstrated here) can be achieved by exchanging air objectives (with identical parfocal distances) using a multi-objective turret, and does not require the immersion chamber to be emptied and re-filled as would be necessary if immersion objectives were used. Fluorescently stained prostate tissues were optically cleared with ethyl cinnamate (n = 1.56) [27] and imaged with 10X and 20X air objectives, using the SIMlens-based light-sheet imaging setup shown in Figure 2.3b. The resolution and FOV achieved by the two objectives are compared in Figure 2.6. Unlike images obtained with the 10X imaging objective, images at 20X reveal sub-nuclear details.

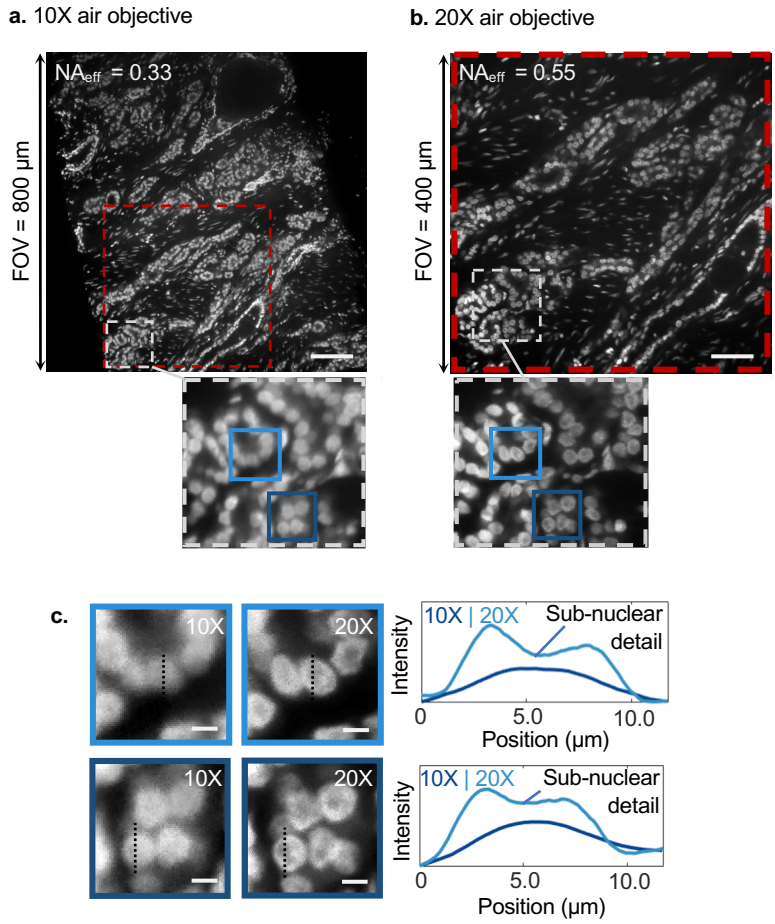

Figure 2.6. (a) A low-magnification view of human prostate tissue cleared and index matched at n = 1.56, fluorescently stained with TO-PRO3, and imaged with a SIMlens and 10X air objective (NA_{air} = 0.21, $NA_{eff.}$ = 0.33). Scale bar is 100 µm. (b) The same region of the tissue imaged at higher magnification, with a 20X air objective (NA_{air} = 0.35, NA_{eff} = 0.55) in conjunction with a SIMlens. Scale bar is 50 µm. (c) Line profiles across individual nuclei demonstrate the resolution

improvement achieved with a 20X objective compared to a 10X objective. Nucleoli are apparent in images obtained with the 20X objective (dark central regions within the nuclei, which are seen as an intensity drop in the line profiles) but are not resolved with the 10X objective. Scale bars are 5 μm. Figure adapted from [34].

Chapter 3. DEVELOPMENT OF A MULTI-RESOLUTION OPEN-TOP LIGHT-SHEET MICROSCOPE

3.1 MOTIVATION FOR MULTI-RESOLUTION IMAGING

As with all imaging techniques, the imaging durations, analysis times, and dataset sizes scale with resolution (to the third power for volumetric imaging). For LSFM imaging with sub-micron resolution (assumed to be isotropic in this simplified example), very large tissue volumes can require hours or even days to image with state-of-the-art sCMOS cameras (< 0.25 mm^3/min for 0.5 μm resolution) in cases that are camera-limited and not photon-limited.

A multi-resolution imaging workflow would greatly improve the efficiency of imaging large tissue volumes in OTLS, as it would enable screening rapidly at low-resolution before selecting regions of interest to image at highest resolution. In clinical practice, multi-resolution workflows are common, in which only localized regions of interest are imaged at the highest levels of resolution. In conventional histopathology, >90% of tissues are surveyed only at low resolution (with 5X to 10X objectives) to rapidly identify suspicious or ambiguous structures. This enables large fields of view to be examined quickly, which is important for tissues/diseases that are spatially heterogeneous and large in extent. In select cases, suspicious or ambiguous regions are then imaged at higher resolution (typically with 20X to 40X objectives) [38]–[41].

Unfortunately, previous OTLS microscope designs (Figure 3.1a-c) have not been ideal for multi-resolution imaging. The SIMlens concept previously described enables the use of readily available and inexpensive air-based objectives for OTLS microscopy (as shown in Figure 3.1d), in which the air-based objectives can be easily interchanged with a motorized turret. Here the optical and mechanical design of this multi-resolution OTLS microscope is described, along with its imaging performance for low- and high-resolution views of thick, intact, optically clear tissues.

To maximize its versatility for clinical and laboratory settings, this system is the most-compact OTLS system to date, measuring approximately 1 x 2 x 1 ft (30.5 x 61.0 x 30.5 cm) in length, width, and height. While the benefits of OTLS microscopy for user-friendly imaging of large and diverse specimens have already been demonstrated, this portable multi-resolution OTLS system will further facilitate the adoption of OTLS microscopy for time- and data-efficient investigations and diagnostics involving large specimens. To practically illustrate these advantages, an example multi-resolution 3D pathology workflow is demonstrated for human prostate carcinoma specimens.

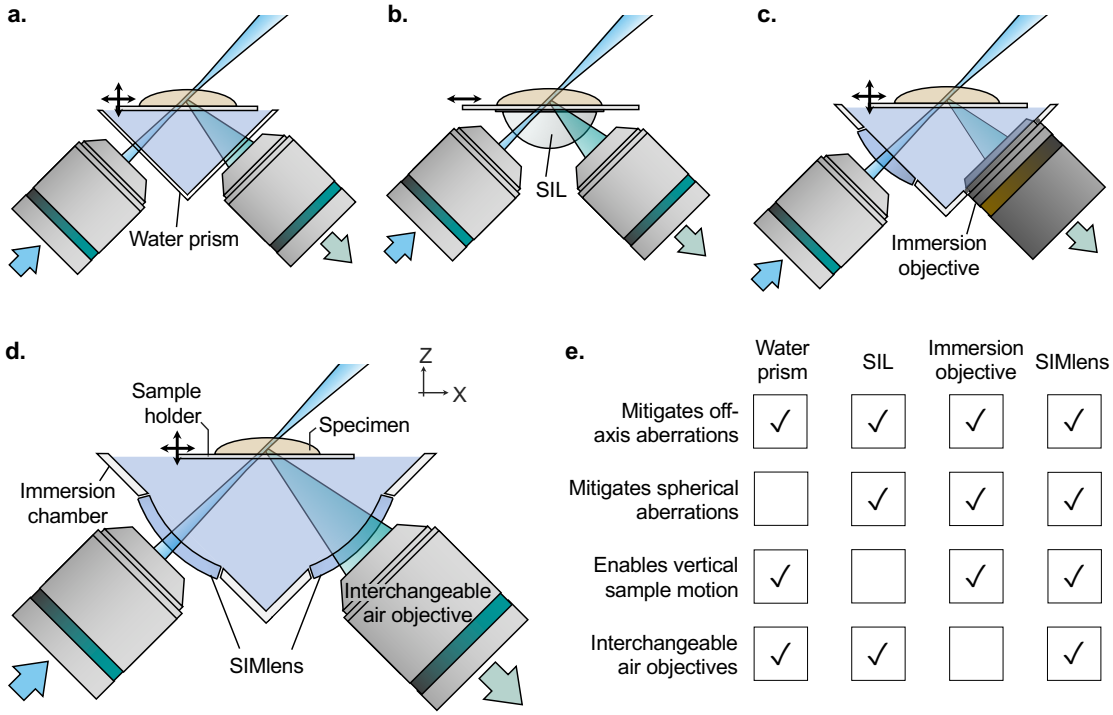

Figure 3.1. (a-c) Previous implementations of OTLS. (a) McGorty *et al.* utilized a water-filled glass prism [25] to reduce off-axis (but not spherical) aberrations. (b) Our first demonstration of OTLS utilized a solid immersion lens (SIL), which mitigates off-axis and spherical aberrations but limits vertical sample motion. (c) A subsequent iteration utilizes an immersion objective [27], which circumvents aberrations but makes it difficult to change objectives. (d) Presented here, a solid immersion meniscus lens (SIMlens) prevents aberrations and enables the use of air-based

objectives for multi-resolution OTLS microscopy [34], [42]. (e) A comparison of wavefront-matching strategies in OTLS microscopy. Figure adapted from [42].

3.2 MAIN BODY DESIGN

Air-based illumination and collection objectives are positioned orthogonal to one another, outside an immersion chamber, and each at a 45° angle relative to the vertical axis (Figure 3.2a). Prior to the air objectives, the respective illumination and collection optics are mounted on breadboards (5” x 12” and 4” x 24”) that are also positioned at a 45° angle relative to the optical table (Figure 3.2b). On the distal side of the air objectives, a pair of SIMlenses (custom fabricated by BMV Optical Technologies for $700/each) are precisely aligned to enable wavefront matching of the focused beams as they transition between air and a higher-index immersion liquid. The SIMlenses are mounted at the interface of a liquid-filled immersion chamber. Above the immersion chamber, a modular sample holder is mounted on a motorized XYZ translation stage (Applied Scientific Instrumentation MS2000, LS-100). The entire OTLS system fits on a 1’ x 2’ breadboard (Thorlabs, MB1224) and can be installed on a portable optical cart (Thorlabs, POC001).

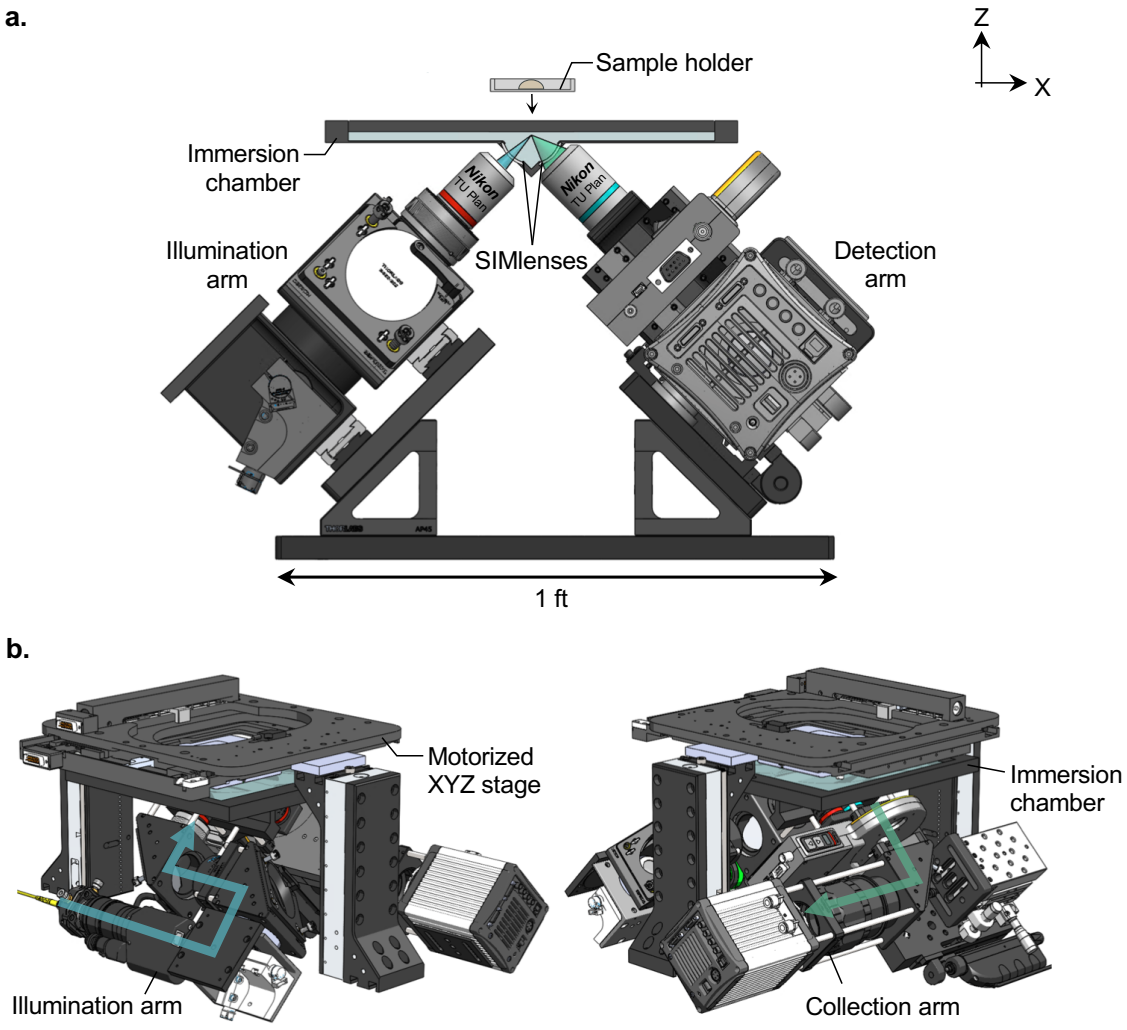

Figure 3.2. Design schematics of the multi-resolution OTLS microscope. (a) Side view of the microscope. Illumination and collection arms are installed on breadboards placed at a 45° angle relative to the vertical axis. Specimens of any size or shape may be placed on a modular sample holder, which is then mounted to a motorized XYZ stage. (b) Isometric views of the microscope showing the illumination arm (left) and collection arm (right). Direction of respective beam paths are shown. Figure adapted from [42].

3.3 SIMLENS DESIGN

The solid immersion meniscus lens (SIMlens) enables wavefront matching of illumination and collection rays as they transition from air-based objectives into the high-index medium contained within the immersion chamber. The SIMlens features two spherical meniscus surfaces, both of

which have a center of curvature that is aligned precisely to the focal point of its accompanying air-based objective, as shown in Figure 3.3a. Rays converging to the focal point are oriented normal to the SIMlens surfaces, enabling them to travel from the air-based objective into the higher-index medium of the immersion chamber (or vice versa) without encountering refractive aberrations.

The SIMlenses on the illumination and collection side are identical (R_1 = 15.5 mm, R_2 = 17 mm, as shown in Figure 3.3a) and were custom fabricated by BMV Optical Technologies. In order to maximize the wavefront-matching performance across the field of view (FOV), the SIMlens radii were designed to be as large as possible without exceeding the working distance (WD) of the objectives (20X WD = 19 mm, 5X WD = 23 mm). Since rays emerging from the edges rather than the center of the FOV are not perfectly normal to the SIMlens surface, a large SIMlens radius relative to the FOV at the focal plane ensures that all rays transition through the SIMlens interfaces at approximately normal angles, where refraction is minimized. Ray-tracing simulations (ZEMAX) demonstrate that diffraction-limited performance is achieved (i.e. a Strehl ratio > 0.80) across the FOV when the SIMlens is paired with the 5X and 20X objectives, as shown in Figure 3.3b. Perfect index matching among the immersion media, sample plate, and sample are assumed for cases including n = 1.33, 1.49, and 1.56 (where FEP film, PMMA, and Hivex [27] may be used as index-matching sample holders in each respective case). Note that the FOV in this case is defined by the size of the camera chip (2048 pixels) and sampling pitch, rather than the FOV of the objective, which is larger. The SIMlens is mounted and sealed at the periphery of the immersion chamber with an off-the-shelf O-ring gasket (The O-Ring Store, Buna-N 70 JIS S16) and retaining ring (Thorlabs, SM19RR), in which the O-ring is robust to a wide range of solvents including ethyl cinnamate (ECi, n = 1.56).

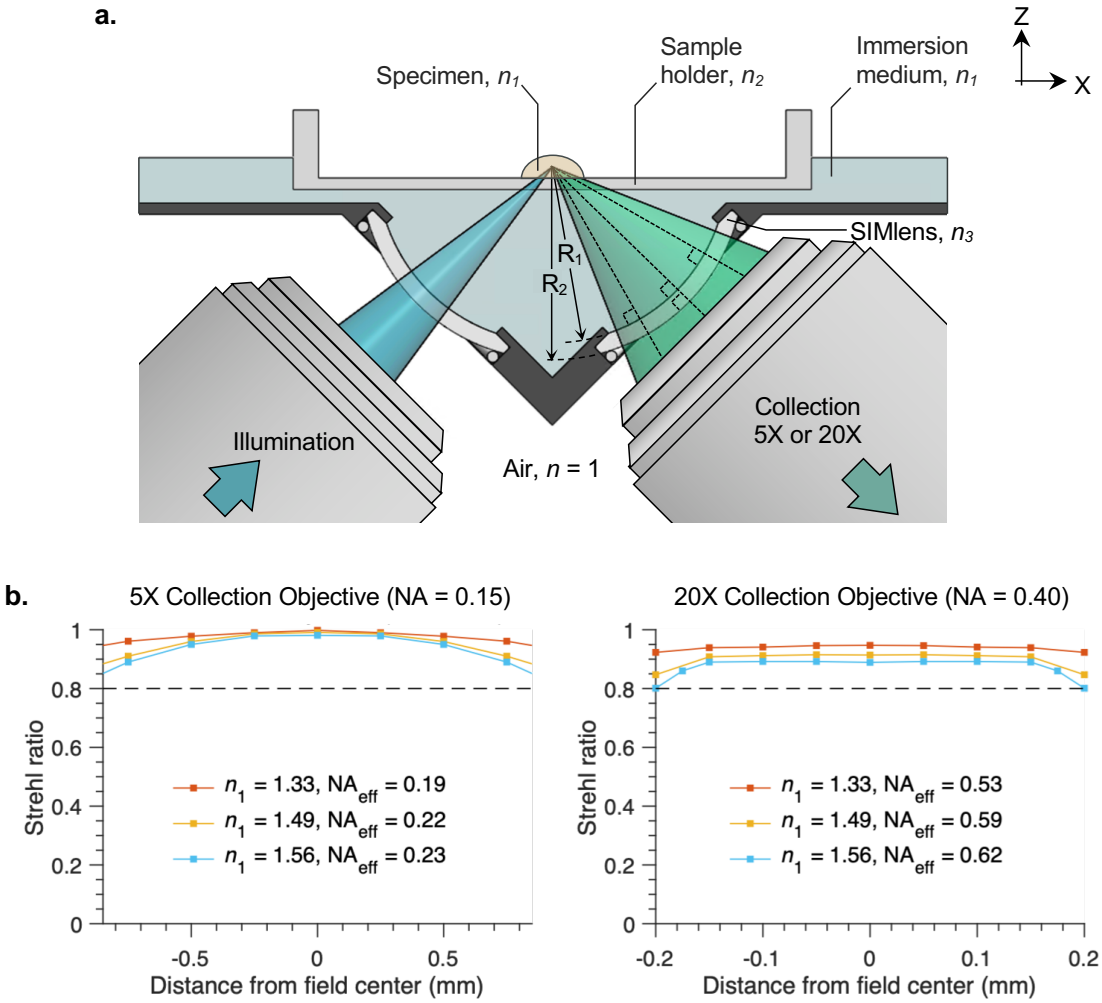

Figure 3.3. Design schematics of the multi-resolution OTLS microscope. (a) Side view of the microscope. Illumination and collection arms are installed on breadboards placed at a 45° angle relative to the vertical axis. Specimens of any size or shape may be placed on a modular sample holder, which is then mounted to a motorized XYZ stage. (b) Isometric views of the microscope showing the illumination arm (left) and collection arm (right). Direction of respective beam paths are shown. Figure adapted from [42].

3.4 ILLUMINATION AND COLLECTION ARMS

On the illumination arm (Figure 3.4a-b), Gaussian illumination is delivered through a single-mode fiber (Thorlabs RGB50HA, NA = 0.12, λ = 488, 561, 660 nm) and is collimated by a 20X objective (Nikon MUL04201, f = 10 mm). A motorized zoom module (Qioptiq FUSION 7:1) expands and

re-collimates the beam, enabling adjustment of light sheet NA to provide a relatively uniform (within the Rayleigh range) light-sheet thickness across the FOV [43] for both low- and high-resolution imaging modes. A pair of orthogonal galvanometric scanning mirrors ("scanning module" in Figure 3.4) is located at a conjugate back focal plane; one mirror scans the point-focused Gaussian beam across the FOV (as a digitally scanned light sheet) [44], whereas the other mirror is used to align the light sheet along the collection path's axial direction. The beam is then relayed by a scan lens (Thorlabs LSM03-VIS, f = 39 mm) and tube lens (Thorlabs TTL100-A, f = 100 mm) to the back focal plane of a 5X objective (Nikon CFI TU Plan Fluor EPI, f = 40 mm). The focusing beam then transitions through the SIMlens into the immersion chamber, and passes through the sample holder into the specimen. For 5X imaging, the effective NA of the light sheet is $NA_1 \sim 0.04$ with a ~5.9-µm thickness (FWHM) and 240-µm depth-of-focus (DOF). For 20X imaging, the effective NA of the light sheet is $NA_2 \sim 0.10$ with a ~2.75-µm thickness (FWHM) and 50-µm DOF.

On the collection arm (Figure 3.4c-d), two air-based objectives (5X Nikon CFI TU Plan Fluor, NA = 0.15 and 20X Nikon CFI TU Plan ELWD, NA = 0.40) are implemented on a motorized linear stage (Newport 436, LTA-HS) that automates the switching between imaging modes. After fluorescence travels through the SIMlens and collection objective (5X or 20X), it is filtered by a motorized filter wheel (Thorlabs FW102C). Band-pass filters are used for the collection of fluorescence excited at one of three wavelengths: 488-nm (Semrock FF01-496/LP-25), 561-nm (Semrock, BLP02-561R-25), and 660-nm (Semrock LP02-664RU-25). Finally, fluorescence is imaged by a tube lens (Thorlabs TTL200-A, f = 200mm) onto a sCMOS camera (Hamamatsu ORCA-Flash4.0 V2). When ethyl cinnamate (ECi) is used as an immersion medium, the 5X objective provides ~1.70 µm lateral resolution (FOV ~ 1.75 mm), whereas the 20X

objective provides ~0.6 µm lateral resolution (~0.40 mm FOV). Note that these lateral-resolution metrics refer to the FWHM dimension of the collection PSF. The actual sampling pitch at the camera is 0.83 µm/px and 0.21 µm/px, respectively (slightly better than Nyquist sampling). The axial resolution of the system is defined by the thickness of the light sheet, which is 5.89 µm and 2.75 µm (FWHM) for low- and high-resolution imaging, respectively.

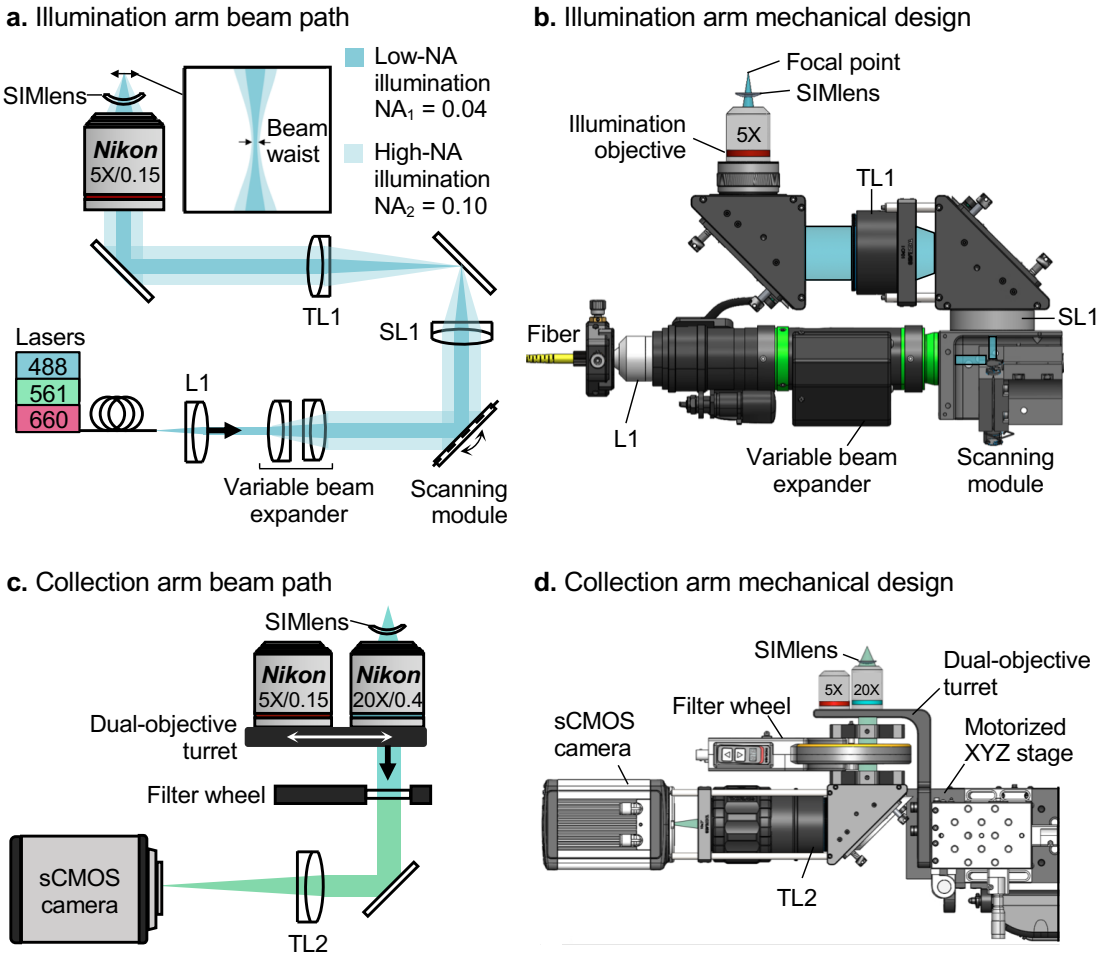

Figure 3.4. (a) Schematic of the illumination arm beam path for both low- and high-NA illumination. (b) Illumination arm CAD. Custom mounting components include the dual-axis galvanometer mount and adapter for SL1 (Hilltop Technology Laboratory, Inc.). (c) Schematic of the beam path for high-NA collection. (d) Collection arm CAD. Custom components include the dual-objective turret and an adapter for the motorized XYZ stage (machined by Hilltop Technology Laboratory, Inc.). Figure adapted from [42].

3.5 SAMPLE HOLDER AND STAGE SCANNING

For sample mounting, a modular transparent holder is suspended below a motorized XYZ stage (Applied Scientific Instrumentation MS2000, LS-100). Optically cleared specimens, such as those treated with CLARITY, CUBIC, or organic solvent-based protocols such as iDISCO [45]–[47], are simply placed on the top surface of the holder which is dipped into the immersion liquid. During imaging, the holder is stage-scanned through the light sheet in three dimensions (XYZ) to create a series of volumetric image strips, which are tiled to create a large volumetric image of the specimen [23], [27]. The scanning and imaging processes are entirely controlled via a Python script, derived from open-source packages and device drivers available on GitHub. Imaging data is compressed by ~10X using B3D compression [48] and stored as 3D datasets in the hierarchical data format (HDF5), which can be interactively viewed in BigStitcher [49]. Volumetric imaging is achieved at a maximum rate of 10 mm^3/min in the low-resolution mode, and 0.13 mm^3/min in the high-resolution mode if B3D compression is not performed. With B3D compression, low- and high-resolution imaging rates are 2.5 mm^3/min and 0.03 mm^3/min, respectively, due to the speed limitations of the B3D program when running on our system which employs a NVIDIA TITAN Xp graphics card with CUDA 10.2.

As mentioned, precise index matching between the sample holder, immersion medium, and specimen is required for aberration-free imaging. Based on ray-tracing analyses (section 3.6), sample-holder materials and thicknesses were chosen to ensure diffraction-limited imaging performance for the chosen clearing protocol(s). For example, for ECi-based clearing [29], a HIVEX (n_2 = 1.56) sample holder with a thickness of 150 µm (custom-machined by BMV Optical Technologies) can be used. Alternatively, 13-µm thick off-the-shelf polyetherimide (PEI, n_2 = 1.69 PolyK Technologies, LLC) films may be used for small or lightweight samples. Both options

achieve near-diffraction-limited imaging (Strehl ratio > 0.80) for NAs of up to 0.625 according to ZEMAX simulation.

3.6 ZEMAX SIMULATIONS

Ray-tracing simulations (ZEMAX) were implemented to characterize device performance. In models of the illumination arm, the initial element is a collimated Gaussian beam located at the scanning module. The diameter of this collimated beam is determined by the NA of the fiber source (NA ~ 0.12), focal length of the collimating objective (f = 10 mm), and magnification setting of the variable beam expander (range 0.35-2.48X), which is used to adjust the beam for the two imaging modes. For low-NA imaging, the Gaussian beam diameter is 0.84 mm ($1/e^2$). The corresponding diameter for high-NA imaging is 2.80 mm. The scanning module is followed by a scan lens (Thorlabs LSM03-VIS, f = 39 mm) and tube lens (Thorlabs TTL100-A, f = 100 mm), which are modeled in ZEMAX as "black box" modules obtained from Thorlabs. Finally, the tube lens is followed by a kinematic mirror, objective (JPO patent JPH11231224), and SIMlens. Spot diagrams of the point-focused Gaussian beam across the FOV indicate that aberrations are minimal for the low- and high-NA light sheets (shown in Figure 3.5).

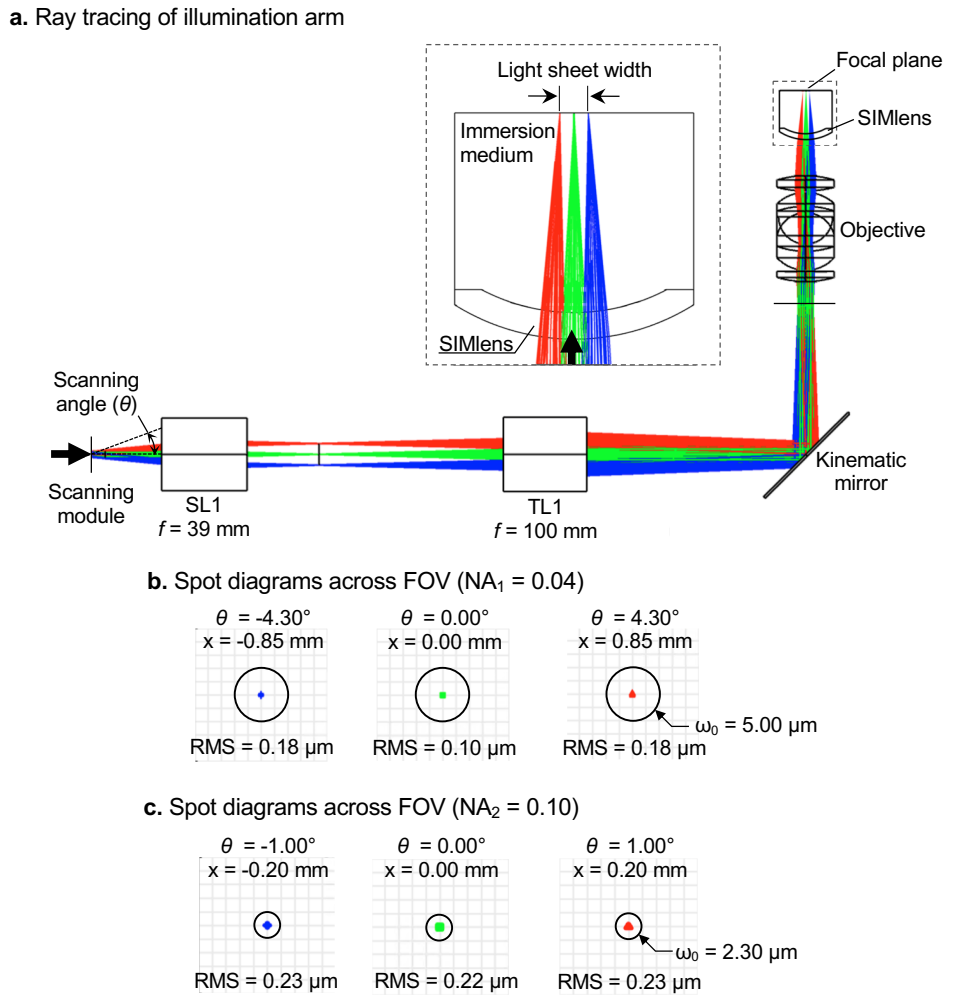

Figure 3.5. (a) To create a digitally-scanned light sheet at the focal plane over time, a mirror scans a Gaussian pencil beam laterally before the beam passes through a scan lens (SL1), tube lens (TL1), objective, and SIMlens. ZEMAX simulations were used to assess spot diagrams of the illumination beam at different points across the FOV. Spot diagrams are shown for different points across the FOV for (b) low-resolution (NA_1) and (c) high-resolution (NA_2) illumination. Note that the black circles in (b) and (c) refer to the size of an ideal Gaussian focus with a $1/e^2$ beam waist radius of ω_o. The spread in the spot diagram is minimal compared to the size of an ideal Gaussian focus, which suggests that the optical performance is near the diffraction limit. "RMS" refers to the root-mean-squared spread in the spot diagrams as shown. Figure adapted from [42].

Ray-tracing simulations were also used to characterize performance of the collection arm (high-resolution mode only, which is more sensitive to aberrations), as shown in Figure 3.6. A

long-working-distance 20X objective (NA = 0.40, f = 10 mm US Patent 7848027B2) was paired with a SIMlens and tube lens (f = 200 mm, Thorlabs TTL200-A). A flat interface, angled at 45° relative to the optical axis, was modeled with various refractive indices and thicknesses (t) to examine the optical tolerance to refractive-index mismatch (Δn) between the sample holder and immersion medium. As has been quantified with previous immersion-based OTLS systems [27], the Strehl ratio was assessed as a function of optical path difference ($\Delta n \times t$) and NA to determine the maximum allowable optical path difference for diffraction-limited imaging. Additionally, the Huygens method in ZEMAX was implemented to simulate point spread functions (PSF).

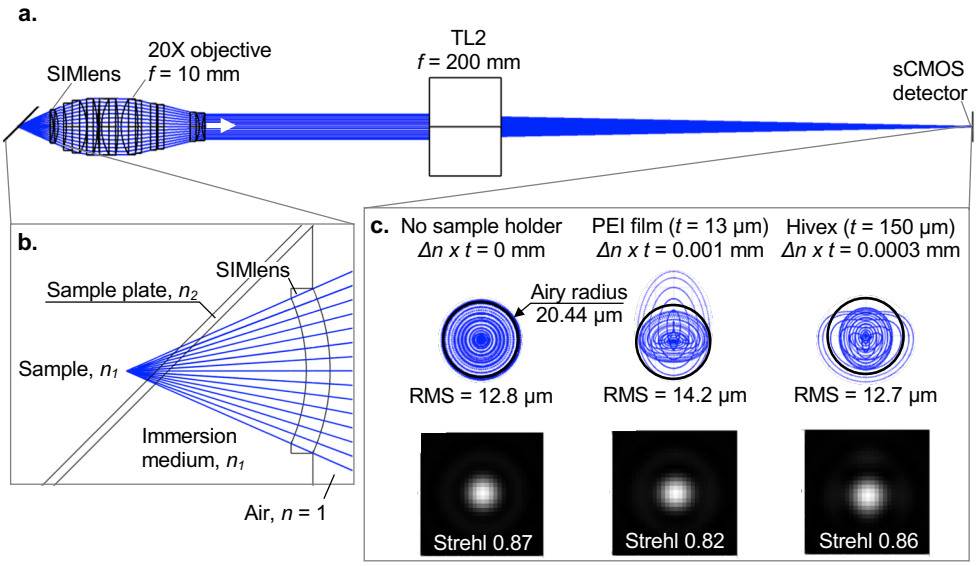

Figure 3.6. (a) In the ZEMAX model of the high-NA collection arm, uniform fluorescence originates at the sample (n_1) and traverses through an angled sample holder (n_2), immersion medium (n_1), and SIMlens before entering the 20X air-based objective. Then, the fluorescence transmits through a tube lens (f = 200 mm) onto a camera (image plane). (b) Enlarged view of the focal region, sample holder (thickness t), and SIMlens. $\Delta n = n_1 - n_2$ is the refractive index mismatch between the immersion media and sample holder, where ideally $\Delta n = 0$. (c) Simulations of the system's spot diagram (top) and PSF (bottom) with an ethyl cinnamate clearing medium (ECi, n_1 = 1.56) and various sample holders are shown. The black circle in the spot diagrams indicates the Airy disk for a uniform beam that is ideally imaged onto the detector plane. The left plot shows simulations with no sample holder ($\Delta n = 0$). The middle and right plots show that when

a PEI film (n_2 = 1.69, 13 μm thick) or Hivex substrate (n_2 = 1.56, 150 μm thick) is used with the ECi clearing medium, they both lead to acceptable imaging performance (Strehl ratio > 0.80). "RMS" refers to the root-mean-squared spread in the spot diagrams as shown. Figure adapted from [42].

3.7 DEVICE PERFORMANCE

To experimentally assess the system's performance in low- and high-resolution imaging modes, sub-diffraction-limited beads were imaged in three dimensions as shown in Figure 3.7. Agarose phantoms (1% w/v) were embedded with a uniform distribution of gold nanoparticles (175 nm diameter), cleared in ethyl cinnamate (ECi), and placed on a 150-μm thick HIVEX sample holder for imaging in an ECi-based immersion bath. Beads were illuminated at 660 nm and imaged in reflectance with both the 5X and 20X objective. Point spread functions (PSF) were averaged among n = 5 beads. The full-width at half maximum (FWHM) intensity profile at 5X was measured to be 1.74 μm in the Y direction, 2.56 μm in the X direction, and 2.51 μm in the Z (vertical) direction, as is shown in Figure 3.7a (coordinate axes shown in Figure 3.3a). As displayed in Figure 3.7b, the FWHM at 20X was measured to be 0.68 μm in the Y direction, 1.09 in the X direction, and 1.07 μm in the Z direction. Note that the worst dimension of the PSF is along the collection axis ("axial" direction). This is determined by the thickness of the illumination light sheet, which is 5.89 μm and 2.75 μm (FWHM) for low- and high-resolution imaging modes, respectively. Note that the term "vertical" is defined with respect to the gravitational axis here.

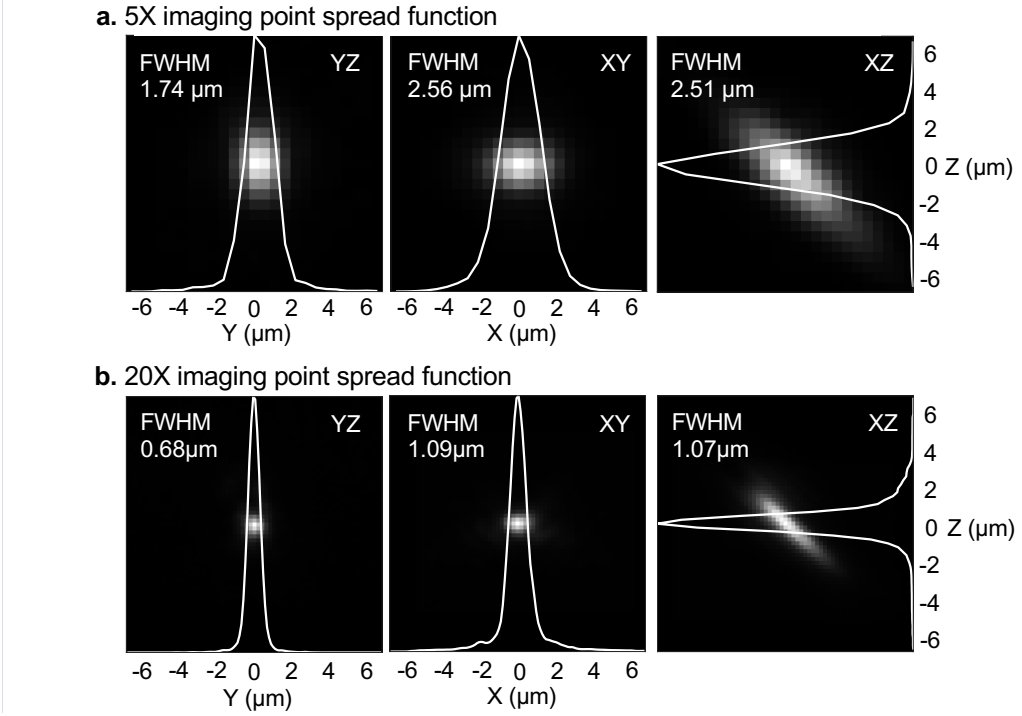

Figure 3.7. Intensity point spread functions (PSFs) obtained by imaging sub-diffraction limited beads in ECi (n_1 = 1.56) at (a) 5X (NA_{eff} = 0.23) and (b) 20X (NA_{eff} = 0.62). Line profiles of the PSFs in the X, Y, and Z directions are used to characterize the resolution of the system. (a) At 5X, the FWHM is 1.74 µm in the Y direction, 2.56 µm in the X direction, and 2.51 µm in the Z direction. (b) At 20X (NA_{eff} = 0.62), the FWHM was measured to be 0.68 µm in the Y direction, 1.09 µm in the X direction, and 1.07 µm in the Z direction. Figure adapted from [42].

3.8 MULTI-RESOLUTION IMAGING OF HUMAN PROSTATE CARCINOMA

We demonstrate the efficiency of this multi-resolution OTLS imaging workflow for the initial identification and then definitive diagnosis of prostate cancer in radical prostatectomy specimens. Slices of fixed prostate tissue (2-3 mm thick) were stained with a fluorescent analog of H&E (TO-PRO-3 and eosin), cleared in ECi (n_1 = 1.56) [29], and placed on a flat HIVEX sample holder (n_2 = 1.56, thickness = 150 µm) for multi-resolution OTLS microscopy [27]. Tissue slices (approximately 30 mm^3 in volume) were first rapidly imaged with the 5X objective (at a volumetric

imaging rate of 2.5 mm^3/min; see section 3.5 for more details). The dataset was immediately viewed in BigStitcher with minimal post-processing to identify regions of diagnostic importance and/or ambiguity. In Figure 3.8, low resolution images that appear to contain tumor infiltrating lymphocytes, blood vessels, and clusters of small glands (potentially carcinoma) are shown. These structures were then imaged in the high-resolution mode to confirm their identity (including diagnosis of the glands). High-resolution imaging is able to resolve flattened endothelial cells that confirm the presence of blood vessels. Additionally, a single layer of epithelial cells with large nucleoli is seen lining the lumen of the small glands, which indicates that these glands are cancerous (lacking a basal cell layer) [39]. Note that the images shown in Figure 3.8 were post-processed with a Beer-Lambert based false-coloring algorithm to mimic the appearance of conventional H&E histology [31], [32].

Imaging the example tissue slice shown in Figure 3.8 in its entirety at high resolution would require at least 3-4 hours at maximum imaging speed. Imaging at low resolution, however, is achieved in a matter of minutes, from which certain diagnostic features of importance or ambiguity can be identified for subsequent localized high-resolution interrogation. It should be noted that 3D volumetric information allows for comprehensive assessment of tissue architecture in a way that traditional slide-based histology cannot achieve. In certain cases where sampling artifacts are known to occur in 2D histology, 3D assessment can potentially improve diagnostic and prognostic interpretation. For example, the grading of prostate cancer can depend upon visualization of "poorly formed glands," the most common Gleason pattern (GP) 4 subtype [50]. GP4 indicates a more aggressive carcinoma than lower GP scores, and is often the threshold at which surgery or radiation therapy is recommended as opposed to active surveillance (for GP3 carcinomas) [51]. However, the appearance of "poorly formed glands" can be due to tangential-sectioning artifacts

in 2D histology [52], as is demonstrated in Figure 3.8b. In this example, a gland that appears to be poorly formed in a single 2D frame (analogous to traditional slide-based histology) is revealed to be fully formed (GP3 rather than GP4) when viewing other depths in the specimen.

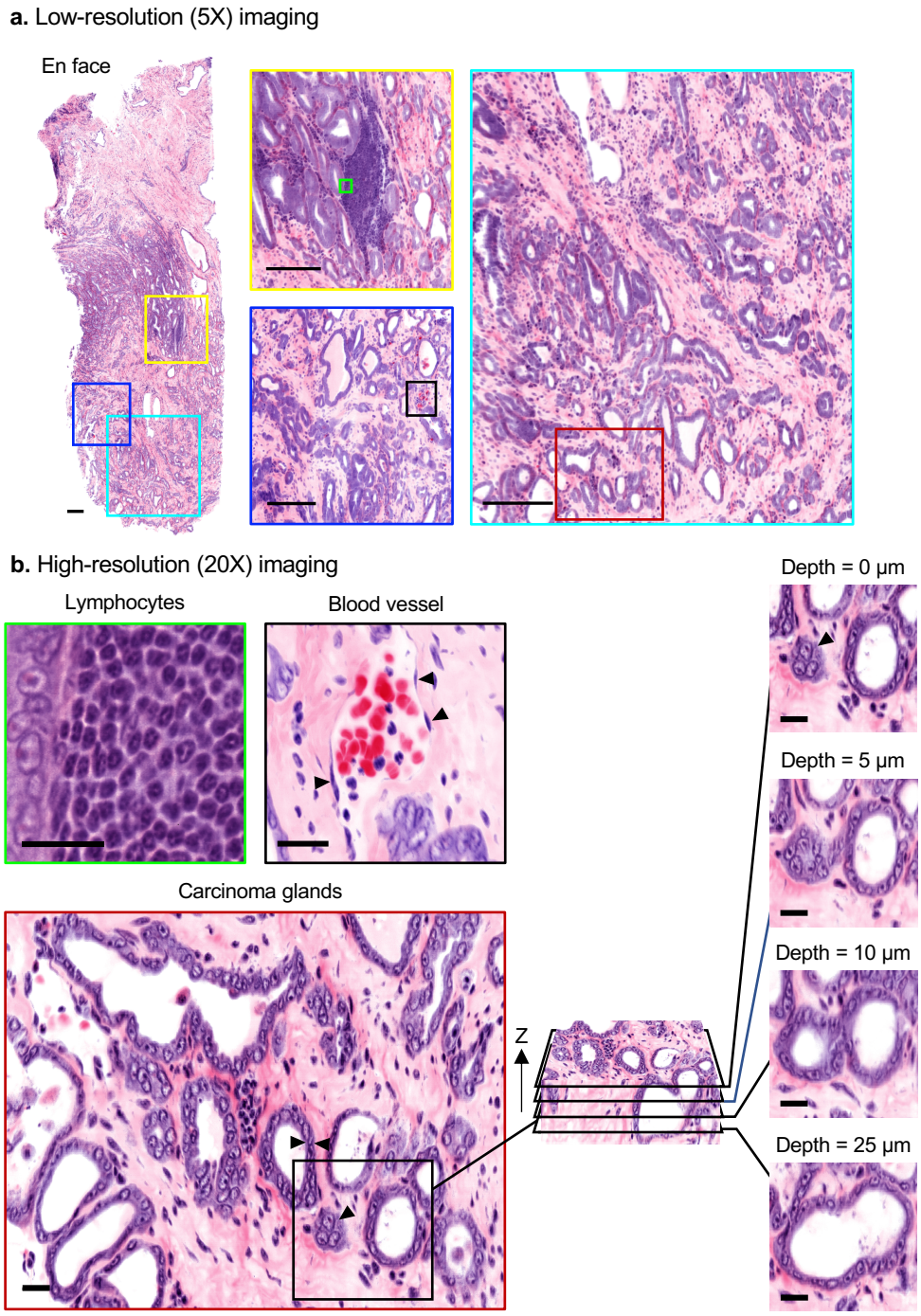

Figure 3.8. Multi-resolution OTLS imaging of human prostate carcinoma. (a) Low-resolution views of a 2.5-mm-thick slice from a prostatectomy specimen that is fluorescently stained with

TO-PRO 3 and eosin, cleared, and then imaged with a 5X air objective. The images are false-colored to mimic the appearance of H&E staining. On the left is an *en face* cross-sectional view of the whole specimen. On the right are regions containing diagnostically important or ambiguous features identified from the low-resolution dataset (at various depths in the specimen). The middle two images appear to contain lymphocytes (green box within yellow box) and a small blood vessel (black box within dark blue box), whereas the image on the right contains many clusters of small glands that appear to be carcinoma (exemplified in the red box within the light blue box). Scale bars represent 200 μm. (b) High-resolution imaging (20X air objective) confirms the identity of these elements. A cluster of lymphocytes is adjacent to carcinoma cells that have large nuclei with prominent nucleoli (top left). Flat endothelial cells of a vessel are seen, adjacent to a small cluster of carcinoma cells (top center). The small glands (bottom left) are lined by a single layer of epithelial cells that have large nucleoli, which is diagnostic of prostate adenocarcinoma (black arrows). To demonstrate the value of 3D information in assessing glandular morphology, which is used to grade the aggressiveness of prostate cancers, a z-stack of images is shown in which a gland appears to be "poorly formed" (Gleason pattern 4) in a single 2D view (black arrow), but is revealed to be a well-formed gland (Gleason pattern 3) when viewing the full 3D dataset (right). Scale bars represent 20 μm. Figure adapted from [42].

Chapter 4. 3D PATHOLOGY OF SENTINEL LYMPH NODES FOR BREAST CANCER STAGING WITH MULTI-RESOLUTION OTLS MICROSCOPY

4.1 MOTIVATION AND BACKGROUND

For the 300,000 patients who are diagnosed with invasive breast cancer or carcinoma *in situ* each year in the United States, the primary treatment method is lumpectomy (breast-conserving surgery) or mastectomy (breast-removal surgery). In addition to removal of the primary tumor, sentinel lymph nodes (LNs) are typically resected during the procedure to facilitate LN staging. The extent of LN metastases is widely regarded as the most important prognostic factor for breast cancer, in part because the spread of cancer to nearby nodes often precedes metastasis to distant organs [53]. Sentinel LNs are evaluated with 2D histology, in which metastatic lesions are classified based on their largest dimension. Metastases may be classified as isolated tumor cells (ITCs; < 200 μm in diameter, or a cluster of fewer than 200 cells), micrometastases (> 200 μm in diameter but < 2 mm in diameter), or macrometastases (> 2 mm in diameter) [54]. The classification of each metastatic lesion determines the assigned LN stage, which indicates the overall status of LN metastases (if present). Typically, if macrometastases are identified (corresponding to stage pN1), patients are treated with complete axillary LN dissection (removal of all axillary nodes).

Although LN staging is one of the most critical components of breast-conserving or breast-removal surgery, the method used for evaluating metastases (conventional histology) is subject to sampling limitations that may lead to under-classification. 2D histology only visualizes a few thin (~ 5 μm thick) sections of each LN specimen (typically ~ 0.5 cm in diameter), in which those thin sections are typically acquired at a spacing (sampling interval) of only a few tens of microns. Collectively, these tissue sections represent < 1% of the specimen. In many cases, histology slides

will show cross sections of tumor deposits at a tangential plane and may under-represent the tumor's largest dimension as illustrated in Figure 4.1.

These limitations motivate the need for a more comprehensive and accurate method of staging LN metastases. There have been efforts to serially section LN metastases for histologic evaluation [3,4]. However, generating and digitally aligning hundreds of glass slides per specimen is a labor- and time-intensive process that is not ideal for clinical settings. Our hypothesis is that classifying lymph nodes with 3D pathology could improve the classification accuracy of nodal metastases in comparison to standard 2D histology, and thereby improve patient treatment.

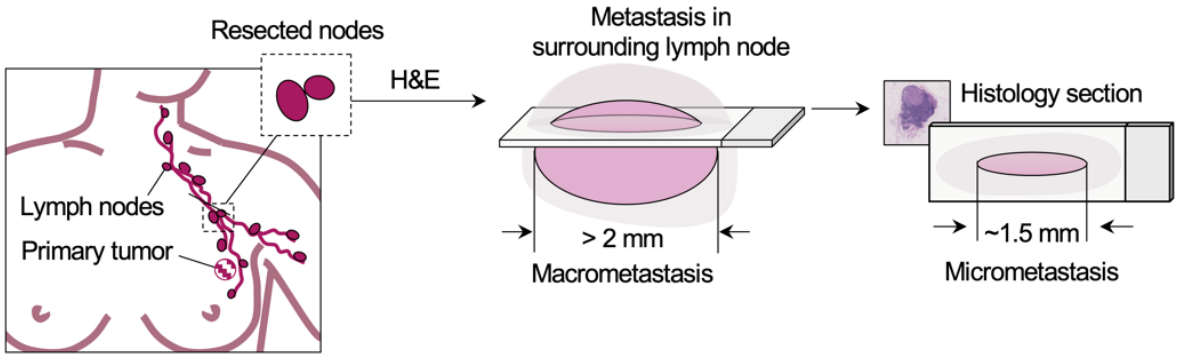

Figure 4.1. Sentinel lymph nodes (LNs) are resected during mastectomy or lumpectomy to facilitate evaluation of nodal metastases. However, sparse sampling with conventional histology may lead to under-classification of metastases in cases for which the maximum diameter of the tumor is not sampled on glass slides. A simplified diagram of a tangentially sectioned metastasis (pink) within surrounding LN tissue (gray) is shown (center). In this example, the 2D section under-represents the largest dimension of metastasis and could lead pathologists to under-classify the metastasis with implications on patient treatment.

4.2 OVERVIEW OF STUDY

As has been previously described, we have developed multi-resolution OTLS microscopy, where whole pathology specimens may be rapidly imaged at low resolution before identifying suspicious regions of interest to selectively image and diagnose at high resolution [42]. Although multi-resolution OTLS microscopy enables multi-scale 3D pathology of large clinical specimens, previously demonstrated pre- and post-imaging workflows (tissue and data processing, respectively) impose limitations that hamper clinical translation. For example, previously reported tissue processing methods are ineffective for certain organs such as lipid-rich lymph nodes (Section 4.3). Additionally, methods for handling large OTLS datasets impose days to weeks of post-processing time before pathologists may interpret the datasets, hindering adoption in time-constrained clinical settings. Here we overcome several of these limitations, developing a comprehensive multi-scale 3D pathology workflow for staging whole LNs. This includes a tissue staining/clearing method for human LNs, multi-scale volumetric imaging with OTLS microscopy, and on-the-fly false-coloring for immediate viewing of H&E-like datasets in 3D [57].

First, we developed an optimized method to stain and optically clear human LN specimens using a fluorescent analog of H&E with CUBIC-HistoVIsion (CUBIC-HV) and tetrahydrofuran-based (THF) permeabilization [58], [59]. This overcomes the staining penetration/uniformity limitations of previously reported methods [27], [60], thus enabling deep 3D imaging of whole LNs. Additionally, we have developed an imaging and computational workflow that enables pathologists to view false-colored datasets (which mimic H&E staining) in 3D immediately after imaging LN specimens with OTLS microscopy. This workflow achieves a 50× reduction in post-processing time compared to our prior reports [12,14], improving feasibility of 3D pathology with OTLS microscopy in routine clinical settings. In this workflow, LN specimens are rapidly imaged

at low resolution and false colored on-the-fly so that pathologists can quickly view the datasets in 3D to identify suspicious or abnormal regions of interest (ROIs). These ROIs are then imaged at high resolution so that pathologists may definitively diagnose each lesion (as a metastasis or benign tissue) and classify metastases as ITCs, micrometastases, or macrometastases. We provide examples in whole LNs for which metastases are diagnosed and classified using our 3D pathology workflow. To evaluate whether 3D pathology may improve staging accuracy in comparison to conventional histology, we compare our 3D pathology results to 2D images that mimic conventional histology. In addition to quantifying the extent to which simulated 2D histology under-estimates the size of metastatic lesions, we highlight two examples for which 3D pathology upstages the results of simulated 2D histology, which could have a significant impact on clinical management.

4.3 A NOVEL FLUORESCENT ANALOG OF H&E ENABLED BY CUBIC-HISTOVISION

A number of methods have been reported for staining fresh and fixed tissues with a fluorescent analog of H&E [15,16]. While these reports utilize small-molecule fluorescent dyes, which are known for rapid and efficient penetration into tissue, the density of lipid-rich membranes in LN tissue [45] impedes penetration and makes it challenging to achieve bright and uniform H&E-analog staining. Here, we describe a protocol that combines CUBIC-HistoVIsion and THF permeabilization for staining thick LN tissues with a fluorescent analog of H&E and optical clearing with CUBIC-R+(N) [58], [59]. This method enables bright and uniform labeling of LN tissues with a nuclear stain by (1) aggressively delipidating the tissue and (2) moderating ionic interactions between the tissue and the positively charged nuclear stain, which allows for more uniform staining as a function of depth. To achieve a bright and uniform cytoplasmic stain (eosin

analog), as reported in [59], we found that incubating AlexaFluor 647 NHS ester in an aqueous/tetrahydrofuran (THF) mixture at a pH of 5 improved penetration in comparison to adjusting buffer pH alone. We showcase the results of this fluorescent H&E analog in Figure 4.2a-b, and we describe our fully optimized protocol in the next paragraphs.

Formalin-fixed paraffin-embedded (FFPE) LN tissues were obtained from breast cancer patients previously treated at the University of Washington Medical Center (UWMC). All specimens were de-identified and transferred to researchers by the NorthWest Biospecimen tissue-bank resource at the UWMC with IRB approval from the UW Human Subjects Division. Per standard clinical practice, all LNs were bisected or cut into thick slices (bread loafs) such that the maximum thickness of each LN specimen was 2 mm. All specimens (bread-loaf slices) from each LN were imaged to enable comprehensive examination of whole LNs. Archived FFPE tissue blocks were de-paraffinized by incubating them at 70 °C for 1 hour and then immersing them in Xylene at 65 °C for 48 hours.

In our fully optimized protocol, LN tissues are first de-lipidated with CUBIC-L for 3 days. After subsequently washing the tissues in PBS, the tissues are stained with 2.5 μM SYTOX-G in Sca*l*eCUBIC-1A with 500mM NaCl at 37 °C for 3 days. Tissues are then incubated with 0.5μg/mL AlexaFluor 647 NHS ester in an aqueous/THF mixture (100 mg/mL THF in PBS) at pH 5 at 37 °C overnight. Finally, after washing in PBS, tissues are incubated in CUBIC-R+(N) for 24 hr for index-matching purposes (optical clearing) before imaging with OTLS microscopy [58], [62]. Note we have also found that the nuclear stain propidium iodide (PI, 60 μg/mL) may also be used as a suitable cost-effective alternative to SYTOX-G.

Compared with previously reported methods for nuclear and cytoplasmic staining, we demonstrate that our staining/clearing protocol achieves improved penetration and uniformity in

human LNs, both for nuclear labeling (Figure 4.2c-f) and cytoplasmic labeling (Figure 4.2g-h). For nuclear labeling, we compare our method to our original H&E-analog staining protocol, in which LN tissues are incubated with 1μM TO-PRO-3 in 70% ethanol pH4 (30% deionized water) for 48 hours [42], [63]. This protocol achieves poor nuclear staining uniformity as a function of depth (Figure 4.2c). We also compare our method to a SWITCH-mediated version of our original H&E-analog protocol, where tissues are incubated in the same buffer as in Figure 4.2c, but with the addition of 10mM sodium dodecyl sulfate (SDS) for the first 24 hours of incubation at 37 °C to inhibit binding and allow TO-PRO-3 to diffuse more readily into the tissue (SWITCH "OFF"). The tissues are then incubated in the staining buffer without SDS for 24 hours at 37 °C to allow TO-PRO-3 to bind to its nucleic-acid targets at depth within the tissue (SWITCH "ON") [60]. While this method greatly improves penetration of the nuclear stain as a function of depth, SDS compromises the integrity of the nuclear stain and increases background fluorescence (Figure 4.2d). Next, we compare our method to the original CUBIC protocol. In this protocol, tissues are pre-treated with CUBIC-1 for 1 day before incubating them with SYTOX-G (2.5 μM) in CUBIC-1 [64]. Staining uniformity as a function of depth in this case is not ideal (Figure 4.2e). Finally, we demonstrate the CUBIC-HV-based method that is used in our optimized protocol. For the nuclear channel (SYTOX-G), this method improves staining penetration and uniformity compared to the methods shown in Figure 4.2c-e, with bright and uniform labeling > 1 mm deep into tissue (Figure 4.2f). For the cytoplasmic channel, we compare the effects of incubating the specimen with AlexaFluor 647 NHS ester in an aqueous/THF mixture compared to staining in an aqueous PBS buffer. In both cases, specimens are incubated with AlexaFluor 647 NHS ester (0.5 μg/mL) in their respective staining buffers (PBS/THF mixture at pH 5 or PBS at pH 5) overnight at 37 °C.

The addition of THF improves tissue porosity and therefore the diffusion rate [59], [65], improving penetration of the NHS ester (Figure 4.2g-h).

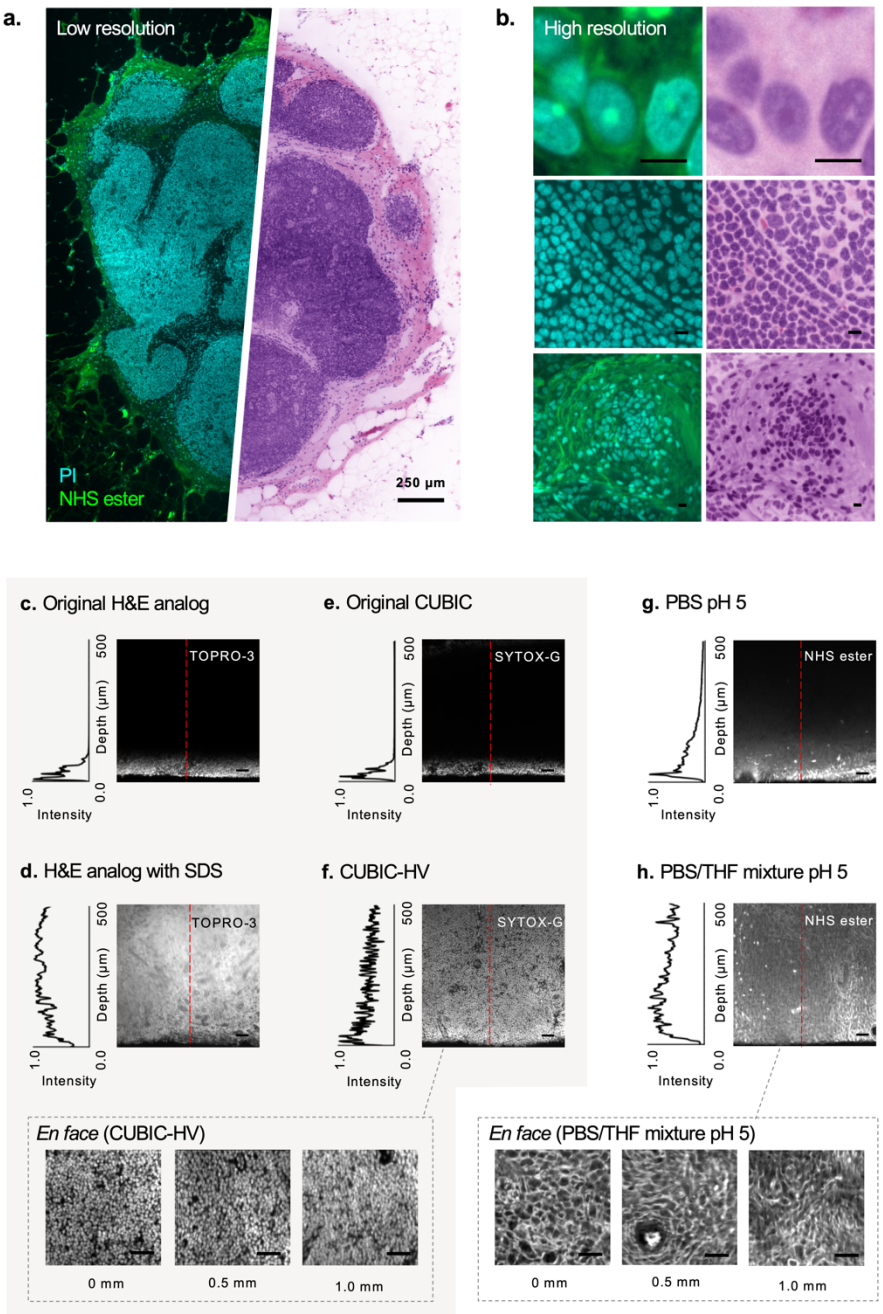

Figure 4.2. (a) En face visualization of a LN stained with our H&E fluorescent analog, cleared with CUBIC-R+(N), and imaged with multi-resolution OTLS microscopy. Standard fluorescence intensity visualization is shown on the left at low resolution. H&E-like visualization is shown on the right, which is generated with an open-source false-coloring code that operates on two-channel

fluorescence images of tissues stained with a nuclear and cytoplasmic fluorophore [31]. (b) Regions of interest shown at high resolution. Standard fluorescence and H&E-like visualizations are shown on the left and right, respectively. Scale bars represent 10 μm. Comparison of various techniques for (c-f) nuclear and (g-h) cytoplasmic staining in LN tissue. Line profiles of staining intensity as a function of depth in the tissue are shown to the left of each vertical cross-section image. For nuclear staining, we show: (c) our original H&E-analog staining protocol, (d) a SWITCH-mediated version of our H&E-analog staining protocol, (e) the original CUBIC protocol, and (f) our final protocol based on CUBIC-HV. At the bottom, en face views are shown at various tissue depths for the dataset in (f). For cytoplasmic staining, we compare: (g) incubating a specimen with our cytoplasmic stain (AlexaFluor NHS ester) in PBS at pH 5, and (h) our final protocol, where the specimen is incubated with the same cytoplasmic stain in a PBS/THF mixture at pH 5. At the bottom, en face views are shown at various tissue depths for the dataset in (h). Scale bars represent 50 μm for vertical cross sections and 25 μm for en face.

4.4 MULTI-RESOLUTION IMAGING WITH OTLS MICROSCOPY

After H&E-analog staining and CUBIC-R+(N) optical clearing, LNs were imaged at low resolution (5× collection objective) with the previously reported multi-resolution OTLS microscope (illustrated in Figure 3.2) [42]. Laser wavelengths of 488 nm and 660 nm were used when detecting fluorescence of SYTOX-G (hematoxylin analog) and AlexaFluor 647 NHS ester (eosin analog), respectively. Bandpass filters (Semrock FF01-496/LP-25 and Semrock LP02-664RU-25) were used for fluorescence detection of SYTOX-G and AlexaFluor 647 NHS ester, respectively. As shown in Figure 4.3 and as previously described for this OTLS system, the refractive index of the sample, sample holder (N-BK7), and immersion medium must be precisely matched for aberration-free imaging. The sample holder is a 0.2 mm-thick substrate made of N-BK7 (n = 1.517, Edmund Optics #66-190). The refractive index of the sample's clearing media is tuned to that of the sample plate (n = 1.517) by adding 0.75 mL of water to 50 mL of CUBIC-

R+(N). For the immersion medium, a 4:3 mixture of silicone oil (n = 1.555, Shin-Etsu HIVAC F-4) and mineral oil (n = 1.467, Sigma-Aldrich CAS 8042-47-5) is used (n = 1.517).

LN specimens were placed on the flat sample plate and imaged at a rate of 10 mm^3/min at low resolution (5× objective) [42]. After low-resolution imaging with our optimized pipeline (described in Section 4.5), the false-colored datasets were viewed in 3D using BigStitcher (an open-source software package in Fiji for efficient visualization of 3D datasets [26,27]) to identify suspicious regions of interest. These regions were then imaged at high resolution (20× objective) at a rate of 0.03 mm^3/min (with B3D compression for high-resolution imaging [48]), false-colored in post-processing, and shown to a pathologist for definitive diagnosis of localized regions in 3D. With our multi-resolution OTLS system, a standard spherically shaped LN with a diameter of 5 mm (volume ~ 65 mm^3) can be imaged at low resolution in ~ 6.5 min whereas high-resolution imaging of such a large volume would require > 8 hours and would generate ~ 80× more data for downstream processing/analysis.

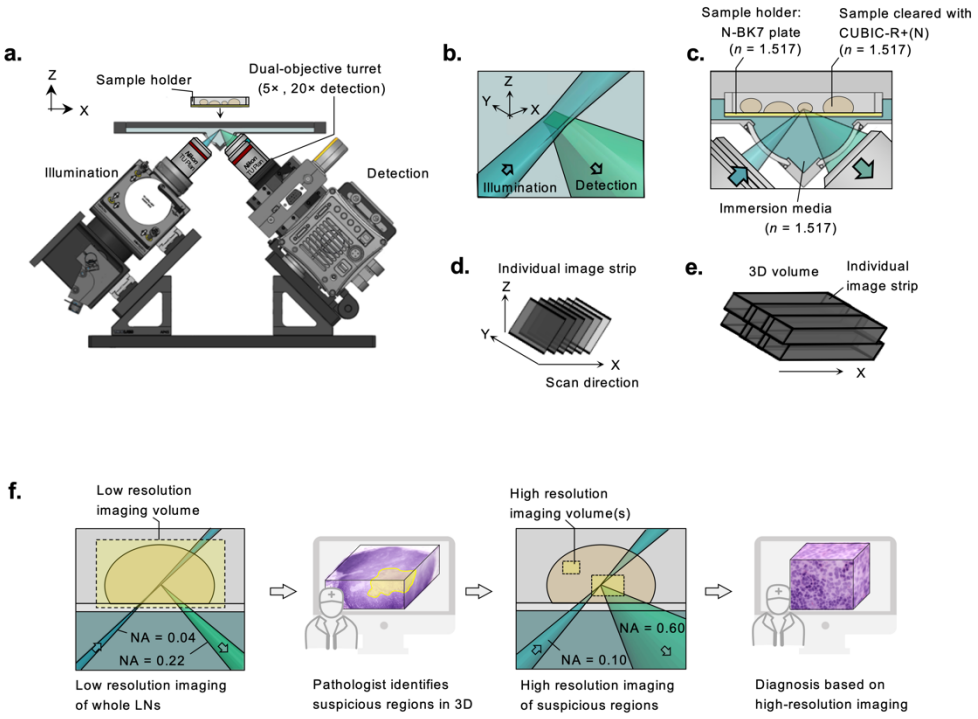

Figure 4.3. (a) Side-view schematic of the multi-resolution OTLS microscope used in this study [3]. The collection arm is equipped with 5× and 20× objectives on a dual-objective turret for low- and high-resolution imaging (respectively). Specimens may be placed on the modular sample holder, which is attached to a motorized stage (not shown) that translates the specimen in XYZ during imaging. (b) Diagram of the focal region within the specimen. (c) To enable aberration-free imaging, the refractive index of the immersion media, sample holder, and sample must be precisely matched. (d) A single 3D image tile is acquired by stage-scanning the specimen in the X direction. (e) Adjacent image tiles are collected in the lateral (Y) and vertical (Z) directions, which are assembled to enable the visualization of a large 3D volume. (f) Diagram of the pathology workflow used for staging axillary LNs from breast cancer patients. LN specimens are imaged at low resolution, false colored to mimic H&E histology, and are viewed by a pathologist in 3D to identify suspicious regions of interest (i.e. possible metastases). These localized regions are subsequently imaged at high resolution in 3D, false-colored, and displayed to a pathologist for definitive diagnosis (tumor vs benign).

4.5 IMAGING AND DATA-PROCESSING WORKFLOW ENABLES VISUALIZATION OF H&E-LIKE DATASETS DATASETS IN 3D

As described in [42], a volumetric image of the specimen is created by stage-scanning the sample through the light sheet in three dimensions to create a series of 3D image tiles that are stored in a hierarchical data format (HDF5). In the post-processing workflow used in our prior studies (Figure 4.4a), the datasets first needed to be fused. Fusion is a processing step performed in BigStitcher [26,27] that blends the seams between overlapping tiles and combines the individual tiles into a contiguous and "seamless" 3D volume. After fusion, the 2-channel datasets (nuclear and cytoplasmic channels) were false-colored in Python to render an H&E-like appearance [31]. False-colored datasets were then saved as a stack of 2D RGB TIFF images, which could be visualized in Fiji after loading the image stack [66]. This workflow (particularly the fusion step) was extremely time consuming and RAM-intensive, requiring 4 hr/mm^3 for low-resolution datasets (3.8 hr/mm^3 for fusion and 6.5 min/mm^3 for false-coloring) on a workstation with an Intel Xeon processor (E5-1620 v4 3.5GHz 4 core), NVIDIA TITAN Xp graphics card, and 128 GB of RAM. Unfortunately, this made it impractical for pathologists to identify suspicious regions of interest from low-resolution datasets within reasonable time frames (while the specimen was still mounted on the OTLS system) for subsequent high-resolution imaging, which hindered feasibility for high-throughput clinical applications.

The workflow we report here bypasses image fusion entirely and false-colors individual 3D tiles on-the-fly as they are acquired (Figure 4.4b). In other words, for each volumetric image tile that is acquired, the camera frames are streamed to RAM as individual 3D tiles and immediately false-colored, resulting in a color (RGB) image tile. The false-colored 3D image tiles are then stored in a HDF5 data container at full resolution and as multiple down-sampled versions

(2×, 4×, and 8×). The associated metadata (position of each tile according to known stage coordinates, sampling intervals, etc.) are also saved in an XML file. After imaging is completed, the datasets are immediately viewable with an H&E-like appearance in BigStitcher, which assembles image tiles in appropriate positions relative to adjacent tiles according to the coordinates in the XML metadata [49]. The HDF5 and XML formats used here are similar to those used in previous reports [14,20] with the exception that three 8-bit color channels (RGB) are saved (for the H&E-false-colored datasets) instead of the two original fluorescence channels (nuclear and cytoplasmic stains). Total imaging times with this new workflow, including on-the-fly false coloring, is ~ 5.1 min/mm^3. Note that our false-coloring algorithm "normalizes" the fluorescence intensities, which degrade slightly as a function of depth, such that the H&E false-colored image outputs are relatively uniform in appearance throughout the 3D datasets. Finally, it should be noted that the use of BigStitcher for visualization of H&E-like images has not been previously reported, as BigStitcher is conventionally used for visualization of standard fluorescence rather than volumetric RGB images. We hope this application will broaden the user base of this versatile open-source 3D visualization platform to clinicians and pathologists.

In summary, our imaging and data-processing pipeline is 50× faster than our previous workflows by omitting fusion, false-coloring individual image tiles on-the-fly (which reduces I/O related latencies associated with false-coloring after the data is saved to disk), and by using a specialized hierarchical image-formatting method for false-colored data to enable volumetric visualization of H&E-like datasets in BigStitcher. Because the fusion process is not performed (i.e. overlapping regions in adjacent image tiles are not blended), visual seams may persist between tiles due to slight offsets (sub-pixel to pixel-level misalignments) between the tiles. However, these minor artifacts do not impede visual interpretation by pathologists. Note that there are also unavoidable

artifacts in conventional 2D histology (cracks, folds, bubbles, etc.). To further reduce processing time, image tiles are binned by 4× in the depth direction (*z* axis) before false-coloring is performed, which results in an effective sampling thickness/interval of ~ 4 μm in the depth direction for each *en face* image (similar to the thickness of H&E slides). Overall, the workflow reported here streamlines pathologist evaluation of low-resolution datasets before localized high-resolution imaging, unhindered by post-processing delays.

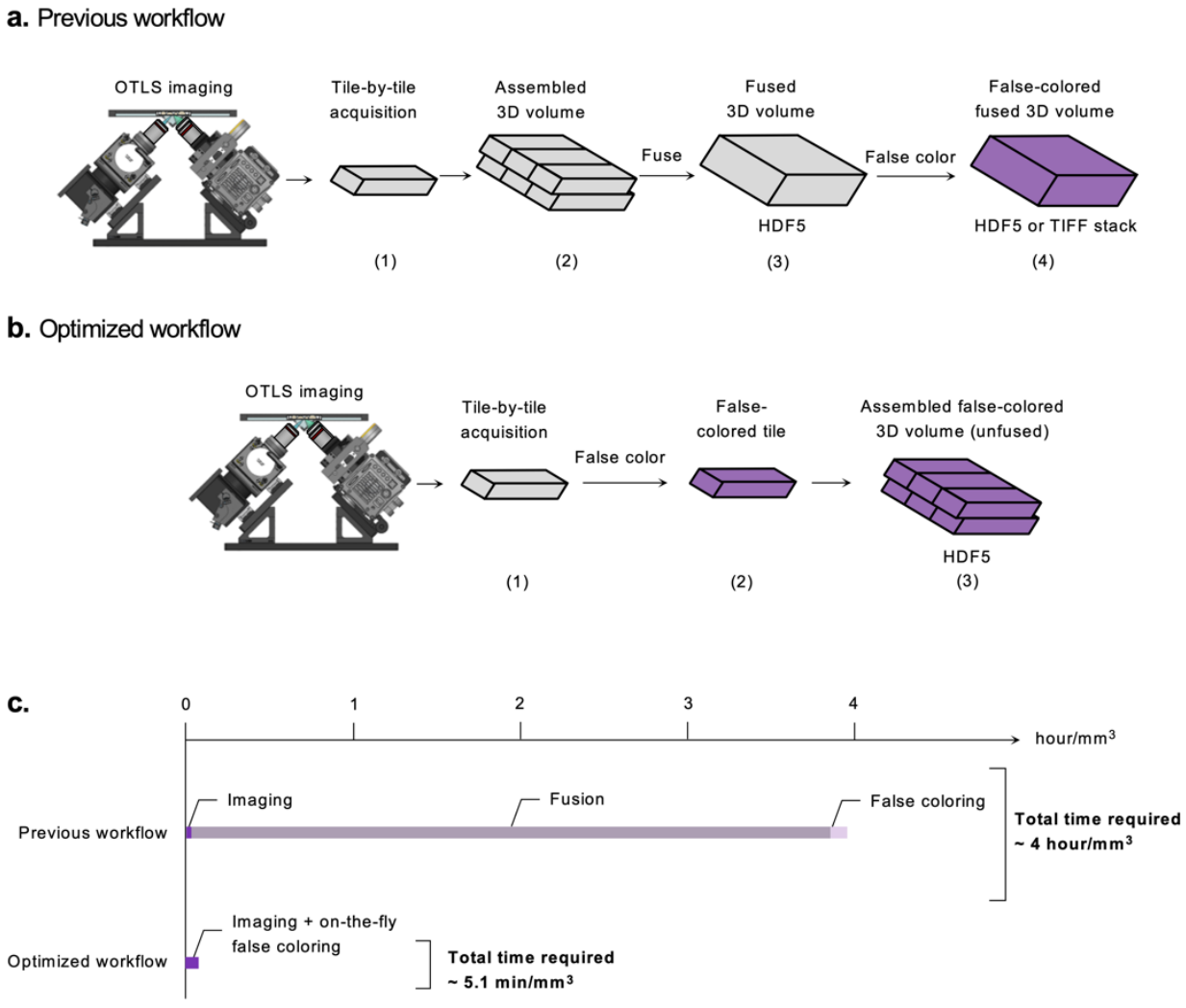

Figure 4.4. (a) Step-by-step illustration of our previously reported workflow [27], [42] for OTLS image acquisition, post-processing, and viewing of false-colored datasets in 3D. A series of

volumetric image tiles were (1) acquired sequentially during imaging and (2) assembled to create a large volumetric image of the specimen. To create a "seamless" 3D dataset, the image tiles were then (3) fused into a single 3D image volume. For visual interpretation, the fused datasets could subsequently be (4) false-colored and saved as a stack of RGB TIFFs (or HDF5). TIFF stacks could then be loaded into Fiji for 3D visualization. (b) The workflow we report here enables H&E-like visualization of 3D image data immediately after imaging. After each 3D image tile is acquired (1), it is (2) immediately false-colored while the raw data is in RAM (before the next tile is imaged) and (3) saved at multiple levels of downsampling in a hierarchical data format (HDF5). After imaging is complete, the volumetric false-colored dataset (hierarchical RGB dataset) may be viewed in BigStitcher with an H&E-like appearance. (c) This new workflow reduces post-processing time by 50× compared to our previous workflow. The time required for each processing step is shown for the previous workflow (top) and optimized workflow (bottom). Here, the reported processing times are for a low-resolution dataset using a workstation equipped with an Intel Xeon processor, NVIDIA TITAN Xp graphics card with CUDA 10.2, and 128 GB of RAM. The time required for false coloring assumes that the depth direction (Z axis) is binned by 4× in all cases.

4.6 LYMPH NODE STAGING 3D PATHOLOGY IMAGE ATLAS

In standard clinical practice, LN metastases are classified based on the largest dimension of the metastasis. Metastases may be classified as isolated tumor cells, (ITCs) micrometastases, or macrometastases. This classification determines pathologic nodal stage (pN0, pN0(i+), pN1(mi), pN1, etc.), where the highest stage reflects the presence of macrometastases and indicates a heavy metastatic nodal burden. This directly informs subsequent treatment decisions; in standard practice, the identification of macrometastases typically results in a decision to perform complete axillary LN dissection (subsequent surgery) to reduce the patient's tumor burden and to improve survival [54], [67], [68].

As was previously described, large LN specimens were deparaffinized, stained with a fluorescent H&E analog (Section 4.3), optically cleared, and then imaged at low resolution

(Section 4.4). False-colored LN datasets (low resolution) were reviewed in 3D in BigStitcher to identify suspicious regions. Suspicious regions of interest were then imaged at high resolution, false-colored, and displayed to a pathologist to definitively diagnose the lesion as a tumor metastasis or benign tissue (Figure 4.5a-b). The metastases were then classified as ITCs, micrometastasis, or macrometastasis based on the largest dimension of the metastatic lesion in 3D using Imaris software (Bitplane). Note that there are slight differences in the amount of shrinkage/deformation in thick tissues processed with our labeling/clearing approach vs. standard FFPE processing (estimated to be within 5% in this study). Future studies should examine and quantify these differences more carefully, and their implications on clinical staging.

4.7 COMPARISON OF 3D PATHOLOGY TO SIMULATED 2D HISTOLOGY

The standard procedure for histologic evaluation of regional LNs includes "facing" into the FFPE blocks (cutting into the tissue block to expose a large surface area of tissue) and then obtaining tissue sections at 3 different "levels" separated by ~ 80 μm, covering a total of ~ 240 μm in depth. Using our volumetric datasets, we mimicked this sampling procedure for 20 LNs by extracting a 2D image cross section at a depth of 500 μm from the tissue surface (similar to how histotechnologists "level" into a tissue block with a microtome) and then extracting two more cross sections at 80 μm intervals (i.e. two additional "levels"). The 2D images (3 levels per LN) were reviewed by a pathologist to diagnose the LN (malignant vs. benign) and classify metastatic lesions. We then compared this to the 3D pathology-based classification for each metastasis. For the 10 nodes that contained metastatic deposits, we found that the 2D *en face* images that mimicked conventional histology underestimated the maximum dimension of the tumor deposits by 19% on average. These results are summarized in Table 1. Additionally, we found that 3D pathology would have led to an upstaging of the LN metastasis in 2 cases (compared to simulated 2D histology). In

both cases, a micrometastasis was observed in the simulated 2D histology images but a macrometastasis (> 2 mm maximum dimension) was evident in the 3D pathology datasets as a result of increased sampling of the specimens. One of these examples is shown in Figure 4.5c.

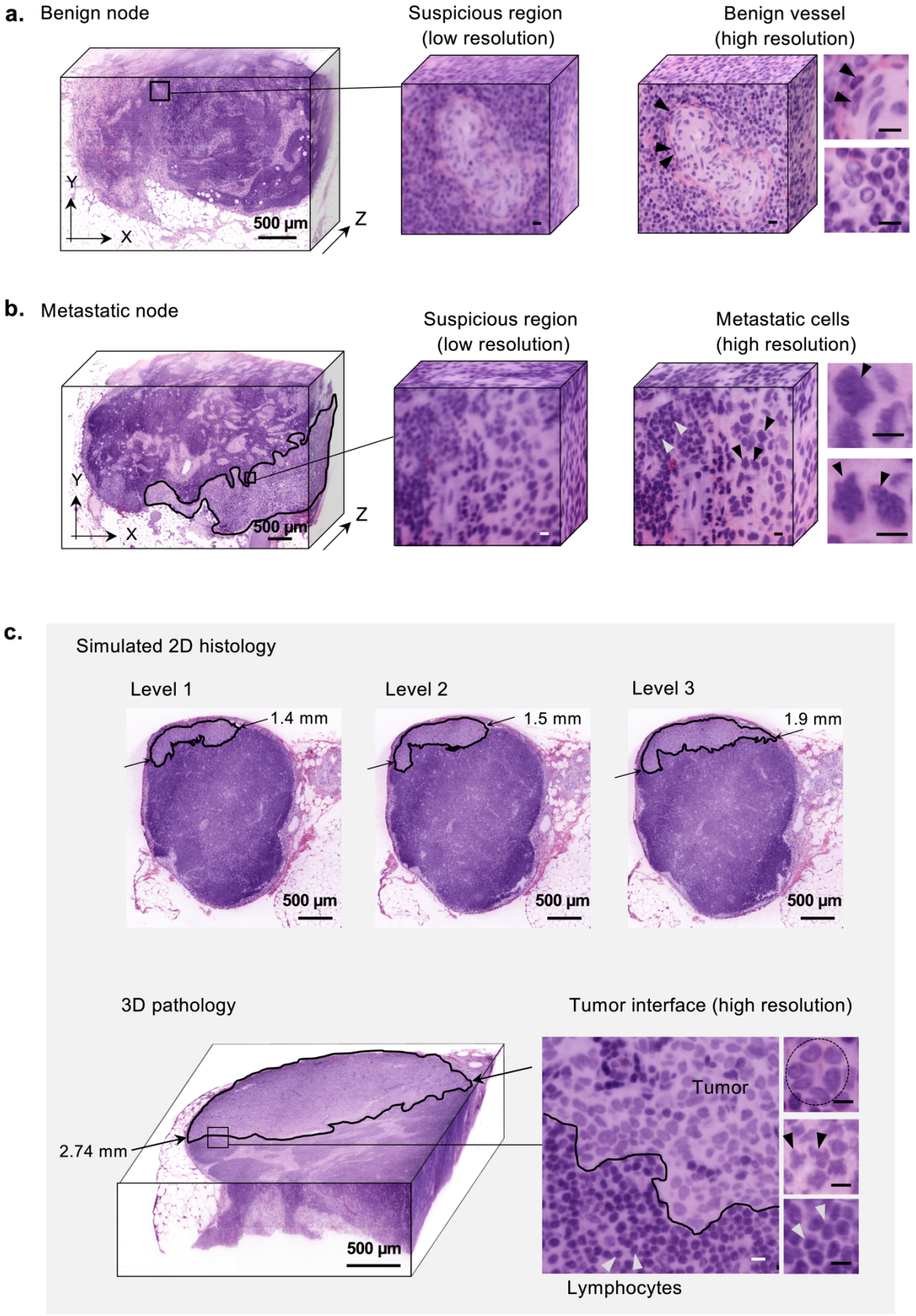
a.
Benign node
Suspicious region
(low resolution)
Benign vessel
(high resolution)
Y
X
Z
500 µm
b.
Metastatic node
Suspicious region
(low resolution)
Metastatic cells
(high resolution)
Y
X
Z
500 µm
c.
Simulated 2D histology
Level 1
Level 2
Level 3
1.4 mm
1.5 mm
1.9 mm
500 µm
500 µm
500 µm
3D pathology
Tumor interface (high resolution)
2.74 mm
500 µm
Tumor
Lymphocytes

Figure 4.5. (a) Image atlas of regional LNs classified with our 3D pathology workflow. Low-resolution images of a benign node (a) and metastatic node (b). For both examples, the low-resolution datasets (left) were used to identify suspicious regions (center). Subsequent high-resolution imaging of those localized regions (right) revealed that the suspicious region in (a) is a benign vessel, as indicated by the flattened endothelial cells lining the vessel, and that the suspicious region in (b) contains cancer cells, as indicated by the enlarged and irregularly-shaped nuclei (black arrows). Lymphocytes adjacent to metastatic cells are indicated by white arrows, exhibiting circular darkly stained nuclei that are densely packed (high nuclear-to-cytoplasm ratios). The maximum dimension of the metastatic nodes is used to classify them as individual tumor cells (< 200 μm), micrometastases (200 μm – 2 mm), or macrometastases (> 2 mm). (c) (Top) A micrometastasis (< 2 mm) is observed in the simulated histology images. (Bottom left) Deep 3D imaging reveals that the tumor deposit is a macrometastasis (> 2 mm), an upstaging that would lead to a more aggressive treatment plan (complete axillary LN dissection). (Bottom right) High-resolution imaging of the interface between the metastasis and benign tissue. Regions of interest show clustered nuclei that are suggestive of tubule formation (top) and enlarged, irregularly shaped nuclei (middle) that are indicative of cancer. A high-resolution view of benign lymphocytes is also shown (bottom, white arrows). Scale bars of regions of interest represent 10 μm.

Node ID	1	2	3	4	5	6	7	8	9	10
Max. dimension based on simulated 2D histology (mm)	4.7	5.5	3.4	6.7	1.9	3.1	5.1	0.3	2.5	6.1
Max. dimension based on 3D pathology (mm)	5.2	6.0	3.5	6.8	2.7	4.0	5.2	2.2	2.8	7.3
% underestimation of max. dimension with 2D histology	9.6	8.0	4.0	1.4	30.3	22.7	2.3	85.4	10.4	15.9

Table 1. The maximum dimension of 10 metastatic LNs was determined by simulated 2D histology and 3D pathology, and the results were compared. On average, simulated 2D histology underestimated the maximum dimension of the metastases by 19%. Additionally, nodes 5 and 8

are examples for which 3D pathology upstaged the diagnosis from a micrometastasis (based on simulated 2D histology) to a macrometastasis (> 2 mm).

4.8 DISCUSSION

One of the most critical components of breast-conserving or breast-removal surgery is staging of LN metastases. The status of regional nodes, or degree of metastatic involvement in regional nodes, directly informs subsequent surgical procedures (axillary LN dissection) and downstream treatment decisions. Unfortunately, the standard of care for staging regional nodes, conventional histology, relies on sparse sampling of the tissue via a few thin tissue sections mounted on glass slides. This 2D-based method is particularly prone to sampling errors because the principal feature for assessing LN metastases (maximum dimension) changes with depth in the specimen. Here, we demonstrate a comprehensive multi-resolution 3D pathology workflow using our previously described multi-resolution OTLS system that enables assessment of whole regional LNs in 3D and overcomes limitations of standard-of-care 2D histology. We showcase a novel fluorescent analog of H&E for staining and clearing of human LNs based on CUBIC-HistoVIsion, overcoming inadequate staining penetration and uniformity seen with alternative staining/clearing techniques. Additionally, we demonstrate a new image-acquisition and false-coloring pipeline that enables pathologists to view H&E-like images of LN tissues interactively in 3D immediately after low-resolution imaging. This allows LNs to be rapidly screened *in toto* at low resolution to identify suspicious regions in 3D. These localized regions may then be imaged at high resolution in 3D, false-colored, and subsequently displayed to the pathologist to facilitate definitive diagnosis and

classification of nodal metastases. This non-destructive 3D pathology method additionally permits downstream molecular assays after OTLS imaging.

Our multi-resolution imaging and data/image-processing processes have been accelerated to enable time- and data-efficient clinical workflows. However, as described in this report, our tissue-staining/clearing protocols, though effective, currently require multiple days. However, this process is largely labor-free and easily automated in a clinical laboratory setting, in which specimens would incubate in specific reagents for hours at a time. Imaging times are important to accelerate so that the imaging device (an OTLS microscope in this case) is not a bottleneck for clinical labs. Likewise, data-processing steps and especially image-interpretation times by pathologists should be minimized because these are costly to scale (i.e. data storage, computational power, and clinician labor). Furthermore, accelerating data/image post-processing times allows pathologists to screen low-resolution H&E-like datasets rapidly (while the specimen is still on the microscope stage) to identify suspicious regions for subsequent high-resolution imaging without having to unmount and remount specimens, which would necessitate complex coordinate-registration and co-registration steps for multi-resolution imaging. In the future, artificial intelligence methods, especially for low-resolution screening of specimens, should be explored to further facilitate rapid LN assessments. Rapid tissue staining/clearing methods may also be possible, as others have been reporting for preclinical research applications [69].

While our study focused on developing a technical workflow for time- and data-efficient 3D pathology of LN specimens, along with a preliminary feasibility study, a number of larger clinical studies are needed to demonstrate value for patient care. For example, studies should be performed to quantify the sensitivity and specificity of tumor detection using both the low-resolution and high-resolution imaging modes, and optimizing these respective

magnification/resolution levels to achieve an ideal trade-off between accuracy and speed for both low-resolution screening of whole LNs and high-resolution definitive diagnosis of suspicious lesions. The ideal multi-resolution workflow should ultimately achieve a high overall accuracy for identifying and classifying LN metastases within a time frame that is "acceptable" to patients, clinicians, and those involved in the economics of healthcare. Furthermore, our multi-resolution 3D pathology workflow should be compared prospectively with true standard-of-care histology practice (rather than simulated 2D histology images in our study) to demonstrate clinical value. While a retrospective analysis of archived tissues would also be of value, there are a number of obstacles. For example, the original histology reports based on the archived specimens used in our study grouped the analysis of multiple LNs into one diagnosis per patient, making it difficult to compare 2D vs. 3D pathology on a per-LN basis. Furthermore, since almost all archived LN tissues are partially consumed for standard histology, subsequent 3D pathology datasets are significantly limited in terms of sampling extent. Future prospective studies comparing 3D vs. 2D pathology should ideally perform non-destructive 3D pathology on whole LN specimens prior to performing standard-of-care slide-based (destructive) histology of those same specimens.

Chapter 5. ENHANCED DETECTION OF NEOPLASIA IN ESOPHAGEAL BIOPSIES VIA NON-DESTRUCTIVE 3D PATHOLOGY WITH DEEP LEARNING TRIAGE

5.1 MOTIVATION AND BACKGROUND

The incidence of esophageal adenocarcinoma (EAC) has been rising dramatically in Western populations over the last several decades. Unfortunately, most EAC patients are diagnosed with late-stage or distant disease for which the 5-year survival rate is < 20% [70], [71]. EAC is believed to arise from Barrett's esophagus (BE), a complication of gastrointestinal reflux disease that results in intestinal metaplasia. BE typically progresses to low-grade dysplasia (LGD) and high-grade dysplasia (HGD) before finally advancing to EAC. Although the risk of progression to EAC is low for patients with BE (0.3% per year), the risk of progression to EAC increases for patients who develop LGD and HGD, for whom the likelihood increases to 2% and > 6% per year, respectively [71]–[74]. Therefore, patients with BE are recommended to receive periodic endoscopic screening for neoplasia (dysplasia or EAC) to enable early detection and intervention, which is key to maximizing patient outcomes [75]. During these screening procedures, 4-quadrant random biopsies are obtained every 2 cm along Barrett's esophagus segments via endoscopic forceps as shown in Figure 5.1 (i.e. Seattle protocol) [70]. In addition to the sampling limitations of random biopsies, the gold-standard method for evaluating these biopsies, slide-based histology, is subject to severe sampling limitations. In conventional histology, biopsy specimens are thinly sectioned, mounted onto glass slides, and stained with hematoxylin and eosin (H&E) to enable microscopic evaluation by pathologists (Figure 5.1). Since this process is destructive to the tissue, only a few tissue sections are typically processed as H&E slides to preserve remaining tissue for downstream

molecular assays if needed. The limited amount of tissue that pathologists view as 2D sections may negatively impact the sensitivity for detecting neoplasia through periodic endoscopic screening [72].

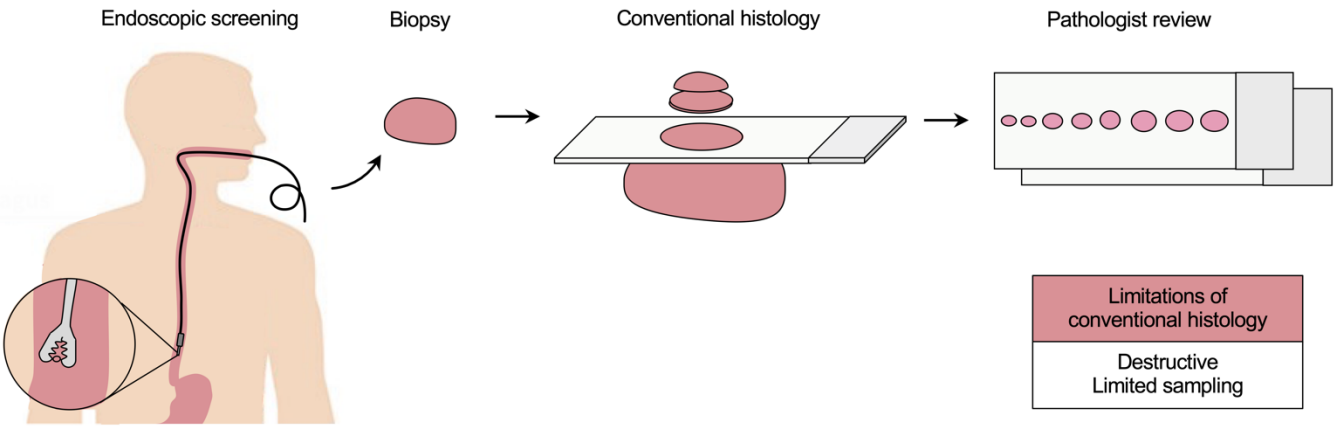

Figure 5.1. During periodic endoscopic screening of Barrett's esophagus patients, 4-quadrant forceps biopsies are taken every 2 cm along the length of the Barrett's esophagus (Seattle protocol). These biopsies are then processed with conventional histology, in which they are thinly sectioned and mounted onto glass slides for H&E staining and pathologist review. With this standard procedure, which is destructive of high-value biopsy specimens, pathologists only visualize a small fraction of the biopsy tissue in the form of 2D slides.

We hypothesize that 3D pathology may improve sensitivity for detecting neoplasia in endoscopic biopsies in comparison to conventional histology since a vastly greater volume of biopsy tissue may be interrogated. Additionally, diagnostically important structures may be observed in 3D, which can reduce certain ambiguities inherent to 2D histology. In this study we utilize the previously described open-top light-sheet (OTLS) microscope as a 3D pathology platform, which enables comprehensive examination of diverse clinical specimens [23].

Importantly, OTLS microscopy is entirely non-destructive to the tissue, which facilitates downstream molecular assays.

Although OTLS microscopy is a non-destructive approach that enables pathologic evaluation of whole biopsies, 3D pathology datasets can be tedious to assess (Figure 5.2a) even at low resolution. Considering that endoscopies alone generate 20 million cases annually in the US for pathologist review [76], diagnostic workflows that take advantage of 3D information without further increasing pathologist workloads would be ideal.

5.2 OVERVIEW OF STUDY

To this end, we have developed an AI-based triage method that guides and streamlines diagnosis of 3D pathology datasets. Our method uses a deep learning algorithm to automatically identify neoplastic regions in small image patches with high sensitivity, and then uses a random forest classifier to aggregate predictions in 3D and select the most important 2D levels (cross sectional images from within the 3D dataset) for pathologist review (Figure 5.2b). Overall, our method reduces the total amount of information (number of 2D images) viewed by pathologists in comparison to standard-of-care histology. In this study, we showcase the performance of our method. In future work we plan to perform a clinical validation study to demonstrate whether AI-assisted 3D pathology improves the sensitivity of diagnosing neoplasia in endoscopic biopsies.

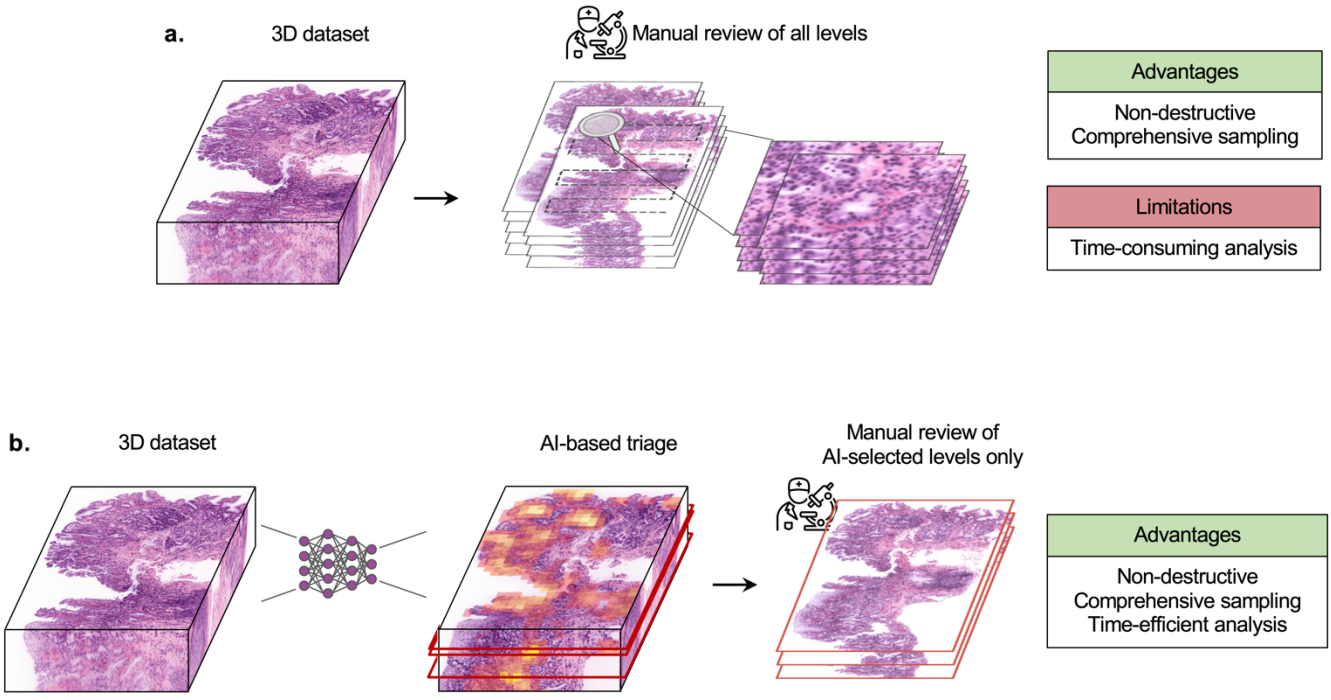

Figure 5.2. (a) Non-destructive 3D pathology provides comprehensive sampling of biopsies while preserving the tissue for downstream processing. However, manually evaluating 3D pathology datasets can be time-consuming. The 3D data (left) may be reviewed by a pathologist as a large stack of 2D images (~ 100 or more levels for 1 mm-thick biopsies). Suspicious regions at each level (center) may need to be viewed at high resolution (right), which can take several minutes per image. (b) Alternatively, AI-assisted triage expedites analysis by utilizing an algorithm to identify neoplastic regions in 3D (center) and then select the levels most likely to contain neoplasia (right) for manual review by a pathologist.

5.3 TISSUE PREPARATION AND OTLS IMAGING

Esophageal biopsy and endoscopic mucosal resection (EMR) specimens were obtained as formalin-fixed paraffin-embedded (FFPE) blocks from the Gastrointestinal Center for Analytic Research and Exploratory Science (GiCaRes) at the University of Washington Medical Center (UWMC). 30 specimens from 11 patients (22 biopsies and 8 EMR specimens) were used for algorithm development. Specimens were deparaffinized by incubating them at 70 °C for 1 hour

and then immersing them in Xylene at 65 °C for 48 hours. Specimens were washed twice in 100% ethanol (EtOH) for 1 hour each, incubated in 70% EtOH (30% deionized water) for 1 hour, then stained with a fluorescent analog of H&E staining by incubating them in 70% EtOH at pH4 (titrated with HCl) with a 1:1000 dilution of TO-PRO-3 and a 1:2000 dilution of Eosin-Y. Finally, the specimens were optically cleared in ethyl cinnamate (n = 1.56) for 4 hours.

Esophageal specimens were then placed on a flat index-matched (n = 1.56) sample plate (Hivex, 200 μm thick) and imaged with a previously reported OTLS microscope using a 20×-objective (NA = 0.40) [42]. A digitally scanned light sheet (NA ~ 0.09) was used to illuminate TO-PRO-3 and Eosin-Y at wavelengths of 660 nm and 488 nm, respectively. Fluorescence was collected with a band-pass filter (Semrock FF01-496/LP-25 and Semrock LP02-664RU-25) and 20× objective (Nikon CFI60 TU Plan ELWD), then relayed to an sCMOS camera as the specimen was stage-scanned in XYZ. Images were collected with an isotropic sampling pitch of 0.21 μm/px. Data was compressed during imaging by ~10× with B3D compression as previously reported [48].

5.4 IMAGE PRE-PROCESSING

Datasets for algorithm development (30 specimens) were processed to facilitate training of the deep learning network (patch-based predictions). First, 1-2 cross-sectional images (2D levels) were selected per specimen for pathologist annotation (43 levels total). Prior to pathologist review, these images were false-colored to mimic an H&E-like appearance [31] and saved in a pyramidal TIFF format. Pixel-level annotations were provided by a board-certified pathologist to indicate regions of neoplasia (dysplasia or cancer) using the Automated Slide Analysis Platform (ASAP). Annotations were recorded in an XML file, where each annotation object was approximated as a polygon with a unique set of vertex coordinates. After annotations were prepared, the images were pre-processed for training the deep learning algorithm. The raw data for both fluorescence

channels (TO-PRO-3 and Eosin-Y) were normalized and saved as an RGB image. The Otsu method was used to threshold and segment the tissue boundaries from the background of the image [77], and overlapping patches (512 × 512 px or ~100 × 100 μm, with 50% overlap between adjacent patches) were extracted from the tissue-containing regions in each 2D image. Finally, each patch was assigned a label of 0 (benign) or 1 (neoplasia) if at least 20% of the image patch was annotated to contain neoplasia (dysplasia or EAC). This procedure generated approximately 393,000 patches (355,800 benign and 37,300 neoplastic) for training.

5.5 CLASSIFICATION FRAMEWORK FOR PATCH-BASED PREDICTIONS

Once OTLS datasets were prepared for network training, a deep learning network (ResNet18, which was pretrained on ImageNet) was trained to label patches as 0 or 1 (benign or neoplastic, respectively) based on the pathologist's ground-truth labels [78], [79]. Image transformations were applied to patches at random during training to improve model performance and to reduce overfitting: image rotations, vertical and horizontal flips, brightness and contrast adjustments, and saturation adjustments. We used a K-fold cross-validation technique to train the model and estimate its overall performance, where the annotated image data was split into K = 15 folds. For each fold, all image patches from 28 specimens were used for training, and patches from the remaining 2 specimens were held out for testing. The model was trained with 20 epochs for each of the 15 folds. Cross-entropy loss was computed after each epoch, which was optimized using stochastic gradient descent during training. Training took approximately 9 hours for each fold on a workstation equipped with a NIVIDIA TITAN Xp graphics card, 128 GB of RAM, and an Intel Xeon processor (E5-1620 v4 3.5GHz 4 core).

For each 2D image, overlapping patch-based predictions were aggregated (overlapping patch regions were averaged) to create a probability heatmap, for which the intensity value of any

given pixel (maximum value of 1.0) represents the predicted probability that the corresponding image patch contains neoplasia. With an overlap value of 50%, the intensity value of each pixel in the heatmap is the average of 4 overlapping patch predictions (except for patches at the boundary of the tissue). Predictions were generated for all 2D levels in each 3D specimen, resulting in a 3D heatmap that predicts the presence of neoplasia within the whole specimen (Figure 5.3b).

5.6 CLASSIFICATION FRAMEWORK FOR IMAGE-LEVEL PREDICTIONS

After patch-based predictions were generated for whole specimens in 3D, we train a random forest classifier (RFC) to select the most important 2D image levels for pathologist review [79]. We extract a set of 3 features from each level of the probability heatmap to serve as inputs to the RFC: the maximum predicted probability in the heatmap, the number of patches for which $P > 0.10$, and the image noise (standard deviation). The RFC then predicts the overall diagnosis of the respective level (benign vs. neoplasia) based on these features. To train the classifier for this task, we use the generated heatmaps that correspond to the 43 image levels annotated by the pathologist (as described in Section 5.4). The ground truth label for each image (or alternatively, for each set of features from the corresponding heatmap) is 0 or 1 according to the annotations, where images that contain a neoplastic annotation are assigned a label of 1 (entirely benign images are assigned a label of 0). Using the same train-test splits described in Section 5.5, we use 15-fold cross-validation to train and evaluate the RFC's performance.

After training the RFC to discriminate between benign and neoplastic levels, we use the classifier to generate predictions on all 2D image levels within whole 3D specimens. The output for each level is a single value (maximum of 1.0) corresponding to the probability that the image contains neoplasia (Figure 5.3c). We sort the levels based on the probability of containing neoplasia, and then identify the top ten levels as the most important images for manual review by

a pathologist (Figure 5.3d). These ten high-priority images are finally false-colored to create an H&E-like appearance for pathologist review [31].

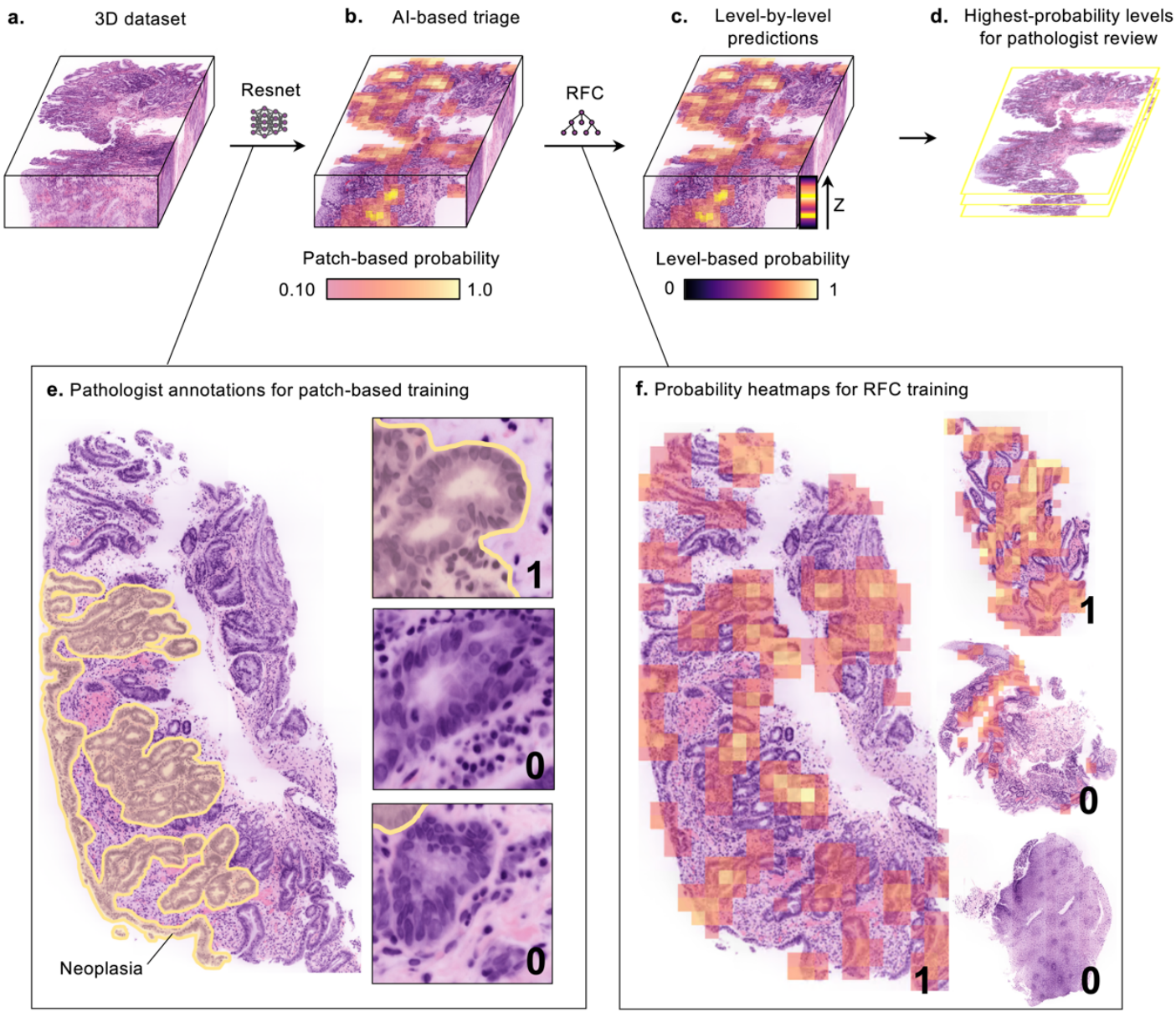

Figure 5.3. (a) For each 3D pathology dataset, a deep-learning algorithm is used to identify neoplastic image patches. These predictions are aggregated in XYZ, resulting in a (b) 3D heatmap that indicates the average predicted probability of each patch containing neoplasia. (c) A random forest classifier then predicts whether each level of the heatmap contains neoplasia. Finally, the levels are sorted based on predicted probability and the (d) 10 highest-ranked images are identified

for pathologist review. (e) The training data used for this prediction pipeline comes from 43 image levels with pixel-level annotations for neoplasia (left). To train the patch-based deep-learning model, these images are split into 100 um x 100 um patches (right) where each patch is assigned a ground truth label of 1 (neoplastic) if at least 20% of the patch contains an annotation for neoplasia (ground truth labels are shown for each patch). (f) After the patch-based algorithm generates probability heatmaps for each annotated image (examples shown), a set of image features are extracted from these heatmaps to serve as inputs into the RFC for training. The 2D image levels are assigned a ground truth label of 0 or 1 according to the pathologist's original annotations, and the RFC is trained to discriminate between benign and neoplastic image levels. For each probability heatmap shown, the respective ground truth label is also shown according to the pathologist's annotations.

5.7 PATCH-BASED AND IMAGE-BASED CLASSIFICATION RESULTS

To demonstrate the performance of the patch-based classifier, we show several examples of 2D heatmaps along with corresponding ground truth annotations (regions encircled by black lines) in Figure 5.4a-c. Each of these heatmaps were generated during the cross-validation testing phase of the patch-based algorithm. We additionally show examples of true positive and true negative patch-based predictions from these examples, as well as the average patch-based receiver operating characteristic (ROC) curve for each of the 2D cross-sectional images.

As shown in Figure 5.4d, the overall performance of the patch-based classifier was benchmarked by computing ROC curves for all 15 cross-validation folds applied to 1-2 image levels from a total of 30 specimens (43 total image levels). The average ROC curve is also shown (AUC = 0.89). On average, the algorithm identifies neoplastic regions with 90% patch-based sensitivity and 71% patch-based specificity (Figure 5.4d), which is deemed adequate for this particular application to screen for the presence of neoplasia in thousands of image patches within hundreds of image levels per 3D pathology dataset.

Finally, we benchmarked the RFC's performance at discriminating between image levels that are entirely benign vs. containing neoplasia. The ROC curve for the classifier's performance is shown in Figure 5.4e, with an AUC = 0.92. Selection of the most-optimal probability threshold yields an overall image-based sensitivity of 87% and specificity of 73%.

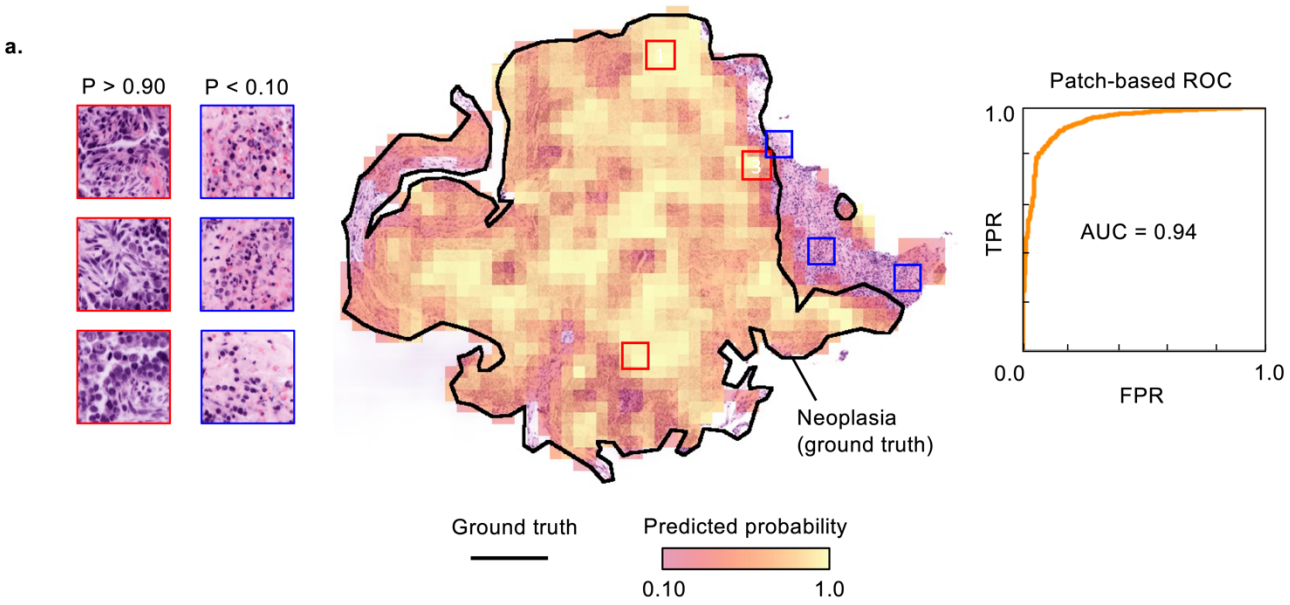
a.
P > 0.90
P < 0.10
1
3
Neoplasia
(ground truth)
Patch-based ROC
1.0
TPR
AUC = 0.94
0.0
1.0
FPR
Ground truth
Predicted probability
0.10
1.0

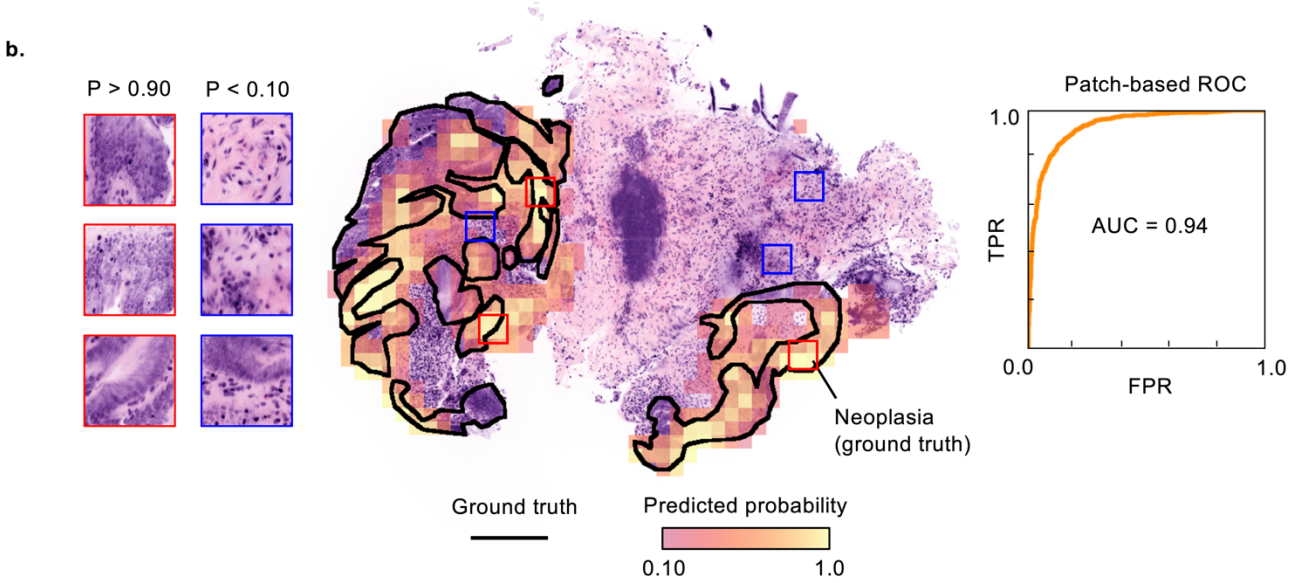
b.
P > 0.90
P < 0.10
Neoplasia
(ground truth)
Patch-based ROC
1.0
TPR
AUC = 0.94
0.0
1.0
FPR
Ground truth
Predicted probability
0.10
1.0

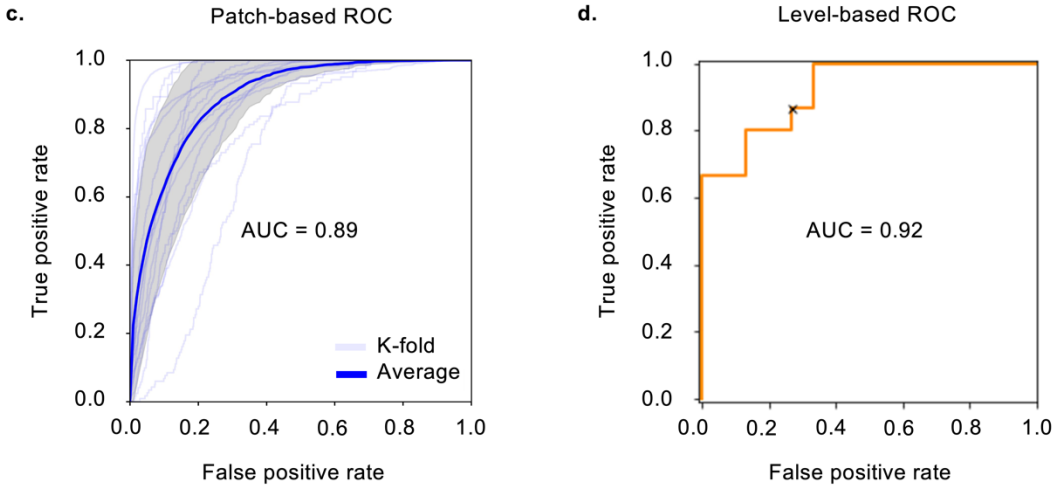
c.
Patch-based ROC
True positive rate
AUC = 0.89
K-fold
Average
False positive rate
d.
Level-based ROC
True positive rate
AUC = 0.92
False positive rate

Figure 5.4. (a-b) Probability heatmaps generated by the patch-based algorithm are overlaid onto OTLS images of biopsy specimens from the annotated image set. These predicted heatmaps were generated by the patch-based algorithm during the testing phase of the cross-validation procedure. Each square "pixel" in the heat map corresponds to one patch, where the value indicates the averaged probability of that patch containing neoplasia (maximum 1.0). The heatmaps are overlaid onto their respective false-colored OTLS microscopy images, and the ground-truth annotations of the neoplastic regions are also shown (regions encircled by black lines). On the left, a few examples of true positive (red outline) and true negative (blue outline) patch-based predictions are shown. On the right, average patch-based ROC curves are also shown for each image. (c) ROC curves are plotted for each cross-validation fold for patch-based predictions, as well as for the average of all 15 folds (dark blue). The standard deviation is shaded in gray. The patch-based algorithm achieves 90% sensitivity and 71% specificity (AUC = 0.89). (d) ROC curve for image-based predictions (RFC) averaged across all 15 cross-validation folds. This image-based classifier achieves 87% sensitivity and 73% specificity (AUC = 0.92).

5.8 FUTURE WORK: PRELIMINARY CLINICAL VALIDATION STUDY

To confirm the clinical value of our method, we aim to compare gold-standard conventional 2D histology to our AI-assisted 3D pathology method using an independent validation cohort of 10 endoscopic biopsies from 10 unseen patient cases (separate from the training cases) imaged with OTLS microscopy. First, a board-certified pathologist will diagnose each biopsy using the described AI-assisted 3D pathology method, i.e. the pathologist will be shown the top ten image levels identified by the algorithm per biopsy. Note that in comparison to gold-standard pathology, in which pathologists at our institution review ~16 tissue sections per biopsy (2 histology slides containing ~8 tissue sections each), this 3D method reduces the total number of images that must be reviewed per biopsy. After performing non-destructive 3D pathology, conventional histology sections will be obtained from the same biopsies according to standard clinical practice (2 histology slides containing ~8 tissue sections each). The pathologist will

diagnose each biopsy based on these slides after a washout period of 2 weeks [80]. We will evaluate whether AI-assisted 3D pathology will upgrade the diagnosis in comparison to conventional histology. An upgrade in diagnosis may indicate that our method improves detection sensitivity of neoplasia in comparison to standard of care while reducing the number of 2D images reviewed by pathologists.

5.9 DISCUSSION

The severe sampling limitations associated with conventional histology may limit the sensitivity for detecting neoplasia through regular endoscopic screening of BE patients. Non-destructive 3D pathology can provide comprehensive visualization of whole biopsies, which may improve detection sensitivity and facilitate earlier intervention. However, it can be time consuming for pathologists to sift through large 3D pathology datasets. To improve diagnostic efficiency, we developed multi-scale OTLS imaging to allow pathologists to quickly view low-resolution information before advancing to high-resolution interrogation of selected regions of interest [42]. However, even low-resolution datasets can be time-consuming to assess for 3D pathology datasets. Therefore, in this report, we have implemented an AI-based triage step to identify the most-important 2D image levels within each 3D dataset for pathologist review. With deep-learning triage of 3D pathology datasets, we reduce the amount of information/images that pathologists must manually review with the potential to improve diagnostic sensitivity in comparison to gold-standard 2D histology. Improved diagnostic sensitivity of EAC and its precursors upon endoscopic screening of BE patients could facilitate earlier therapeutic interventions that are key to improving patient survival.

One of our main priorities in developing a highly sensitive AI-based screening tool was to design a diagnostic workflow that is simple and convenient to pathologists. Particularly, a method that can seamlessly incorporate into pathologist workflows without additional time or training will help to facilitate adoption of 3D pathology into clinical settings. This motivated our choice to provide pathologists with 2D images from the 3D datasets (rather than image stacks or videos of 3D data, for example). Since pathologists are accustomed to reviewing 2D H&E slides, this format allows the pathologist to make a 3D-pathology-facilitated diagnosis without adjusting to a new visualization format. It should be noted, however, that pathologist review of structures in 3D may enhance diagnostic accuracy, especially for structures that can be ambiguous when viewed as 2D cross-sectional images [52], [81], [82] . Therefore, in the future, we plan to explore displaying high-priority 3D image regions as image stacks or volumetric renderings.

Chapter 6. CONCLUSION

Open-top light sheet microscopy has been previously developed for rapid 3D imaging of large pathology specimens [23]. In this report, we summarize development of multi-resolution OTLS microscopy enabled by a solid immersion meniscus lens (SIMlens) for OTLS [34], which alleviates limitations of previous OTLS architectures and conveniently enables multi-resolution imaging [42]. This compact OTLS system is particularly promising for translation of 3D pathology into clinical settings, as it enables users to rapidly transition between low- and high-resolution views for efficient screening which is vital to current pathology workflows. We demonstrate how 3D pathology with multi-resolution OTLS microscopy may improve breast cancer staging accuracy and management of breast cancer patients. As part of this work, we develop a comprehensive 3D pathology workflow for screening whole lymph nodes enabled by a novel

fluorescent analog of H&E staining for lipid-rich tissues, and a rapid acquisition and post-processing workflow that allows pathologists to visualize false-colored 3D pathology datasets immediately after OTLS imaging. Finally, to streamline 3D pathology, we summarize development of a deep learning-based computational method that automatically segments potentially neoplastic regions for pathologist review. We showcase performance of this AI-assisted 3D pathology method and discuss our future aim to determine whether this diagnostic workflow facilitates improved detection sensitivity of neoplasia through surveillance endoscopy of Barrett's patients.

BIBLIOGRAPHY

[1] "Cancer Facts & Figures 2020," *American Cancer Society*. (2020).

[2] M. Comanescu, L. Annaratone, G. D'Armento, G. Cardos, A. Sapino, and G. Bussolati, "Critical steps in tissue processing in histopathology," *Recent Patents DNA Gene Seq.*, 6 (1) , 22–32 (2012).

[3] T. A. Ozkan, A. T. Eruyar, O. O. Cebeci, O. Memik, L. Ozcan, and I. Kuskonmaz, "Interobserver variability in Gleason histological grading of prostate cancer," *Scand. J. Urol.*, 50 (6), 420–424 (2016).

[4] J. K. McKenney *et al.*, "The potential impact of reproducibility of gleason grading in men with early stage prostate cancer managed by active surveillance: A multi-institutional study," *J. Urol.*, 186 (2), 465–469 (2011).

[5] J. I. Epstein *et al.*, "A Contemporary Prostate Cancer Grading System: A Validated Alternative to the Gleason Score," *Eur. Urol.*, 69 (3), 428–435 (2016).

[6] V. Parkash, C. Bifulco, R. Feinn, J. Concato, and D. Jain, "To count and how to count, that is the question: Interobserver and intraobserver variability among pathologists in lymph node counting," *Am. J. Clin. Pathol.*, 134 (1), 42–49 (2010).

[7] F. Fereidouni *et al.*, "Microscopy with ultraviolet surface excitation for rapid slide-free histology," *Nat. Biomed. Eng.*, 1 (12), 957–966 (2017).

[8] J. Li, P. Lin, Y. Tan, and J.-X. Cheng, "Volumetric stimulated Raman scattering imaging of cleared tissues towards three-dimensional chemical histopathology," *Biomed. Opt. Express*, 10 (8), 4329 (2019).

[9] R. M. Nolan *et al.*, "Intraoperative optical coherence tomography for assessing human lymph nodes for metastatic cancer," *BMC Cancer*, 16 (1), 1–10 (2016).

[10] T. T. W. Wong *et al.*, "Fast label-free multilayered histology-like imaging of human breast cancer by photoacoustic microscopy," *Sci. Adv.*, 3 (5) (2017).

[11] M. Ragazzi *et al.*, "Fluorescence confocal microscopy for pathologists," *Mod. Pathol.*, 27 (3) 460–471 (2014).

[12] B. Hu, D. Bolus, and J. Brown, "Dual-view inverted selective plane illumination microscopy (diSPIM) with improved background rejection for accurate 3D digital pathology," *SPIE*, 1049 (2018).

[13] E. G. Reynaud, J. Peychl, J. Huisken, and P. Tomancak, “Guide to light-sheet microscopy for adventurous biologists,” *Nat. Methods*, 12 (1), 30–34 (2015).

[14] R. M. Power and J. Huisken, “A guide to light-sheet fluorescence microscopy for multiscale imaging,” *Nat. Methods*, 14 (4), 360–373 (2017).

[15] J. Huisken, J. Swoger, F. Del Bene, J. Wittbrodt, and E. H. K. Stelzer, “Optical Sectioning Deep Inside Live Embryos by Selective Plane Illumination Microscopy,” *Science* (305), 1007–1009 (2004).

[16] R. Tomer, K. Khairy, F. Amat, and P. J. Keller, “Quantitative high-speed imaging of entire developing embryos with simultaneous multiview light-sheet microscopy,” *Nat. Methods*, 9 (7), 755–76 (2012).

[17] H. U. Dodt *et al.*, “Ultramicroscopy: Three-dimensional visualization of neuronal networks in the whole mouse brain,” *Nat. Methods*, 4 (4), 331–336 (2007).

[18] Y. Wu *et al.*, “Inverted selective plane illumination microscopy (iSPIM) enables coupled cell identity lineaging and neurodevelopmental imaging in Caenorhabditis elegans,” *Proc. Natl. Acad. Sci. U. S. A.* 108 (43), 17708–17713 (2011).

[19] M. B. Bouchard *et al.*, “Swept confocally-aligned planar excitation (SCAPE) microscopy for high-speed volumetric imaging of behaving organisms,” *Nat. Photonics*, 9, 113–119 (2015).

[20] B. Migliori *et al.*, “Light sheet theta microscopy for rapid high-resolution imaging of large biological samples,” *BMC Biol.*, 16 (57), 1–19, (2018).

[21] T. Chakraborty *et al.*, “Light-sheet microscopy of cleared tissues with isotropic, subcellular resolution,” *Nat. Methods*, 16, 1109–1113 (2019).

[22] R. Tomer and K. Deisseroth, “Rapid High-resolution Brain Mapping with CLARITY Optimized Light Sheet Microscopy (COLM),” *Microsc. Microanal.*, 21, 717–718 (2015).

[23] A. K. Glaser *et al.*, “Light-sheet microscopy for slide-free non-destructive pathology of large clinical specimens,” *Nat. Biomed. Eng.*, 1, 1–10 (2017).

[24] Y. Chen *et al.*, “Rapid pathology of lumpectomy margins with open-top light-sheet (OTLS) microscopy,” *Biomed. Opt. Express*, 10 (3), 1257–1272, (2019).

[25] R. McGorty, H. Liu, D. Kamiyama, Z. Dong, S. Guo, and B. Huang, “Open-top selective plane illumination microscope for conventionally mounted specimens,” *Opt. Express*, 23 (12), 16142–16153 (2015).

[26] P. Strnad *et al.*, “Inverted light-sheet microscope for imaging mouse pre-implantation development,” *Nat. Methods*, 13 (2), 139–142 (2016).

[27] A. K. Glaser *et al.*, “Multi-immersion open-top light-sheet microscope for high-throughput imaging of cleared tissues,” *Nat. Commun.*, 10 (2781), 1–8 (2019).

[28] R. Mcgorty, D. Xie, and B. Huang, “High-NA open-top selective-plane illumination microscopy for biological imaging,” *Opt. Express*, 25 (15), 17798–17818 (2017).

[29] A. Klingberg *et al.*, “Fully automated evaluation of total glomerular number and capillary tuft size in nephritic kidneys using lightsheet microscopy,” *J. Am. Soc. Nephrol.*, 28, 452–459 (2017).

[30] G. S. Kino, “Applications and theory of the solid immersion lens,” *SPIE*, 3609, 56–66 (1999).

[31] R. Serafin, W. Xie, A. K. Glaser, and J. T. C. Liu, “FalseColor-Python: A rapid intensity-leveling and digital-staining package for fluorescence-based slide-free digital pathology,” *PLoS One*, 15, 1–17 (2020).

[32] M. G. Giacomelli *et al.*, “Virtual hematoxylin and eosin transillumination microscopy using epi-fluorescence imaging,” *PLoS One*, 11 (8), 1–13 (2016).

[33] L. A. Barner, A. K. Glaser, L. D. True, N. P. Reder, and J. T. C. Liu, “A solid immersion meniscus lens (SIMlens) for open-top light-sheet microscopy.”

[34] L. A. Barner, A. K. Glaser, L. D. True, N. P. Reder, and J. T. C. Liu, “Solid immersion meniscus lens (SIMlens) for open-top light-sheet microscopy,” *Opt. Lett.*, 44 (18), 4451–4454 (2019).

[35] S. W. Smith, *The Scientist and Engineer’s Guide to Digital Signal Processing*. California Technical Publishers (1997).

[36] M. Duocastella *et al.*, “Combination of scanning probe technology with photonic nanojets,” *Sci. Rep.*, 7 (3474), 1–7 (2017).

[37] L. Gao, “Extend the field of view of selective plan illumination microscopy by tiling the excitation light sheet,” *Opt. Express*, 23 (5), 6102–6111 (2015).

[38] M. N. Gurcan, L. Boucheron, A. Can, A. Madabhushi, N. Rajpoot, and B. Yener, “Histopathological Image Analysis: A Review,” *IEEE Rev. Biomed. Eng.*, 2, 147–171 (2009).

[39] C. Magi-Galluzzi, “Prostate cancer: diagnostic criteria and role of

immunohistochemistry," *Mod. Pathol.*, 31, S12–S21 (2018).

[40] A. H. Scheel *et al.*, "Physical basis of the 'magnification rule' for standardized Immunohistochemical scoring of HER2 in breast and gastric cancer," *Diagn. Pathol.*, 13 (19), 1–7 (2018).

[41] D. W. et al Tad T. Brunyte, Ezgi Mercan, "Accuracy is in the Eyes of the Pathologist: The Visual Interpretive Process and Diagnostic Accuracy with Digital Whole Slide Images," *J. Biomed. Inform.*, 66 (3), 171–179 (2017).

[42] L. A. Barner, A. K. Glaser, H. Huang, L. D. True, and J. T. C. Liu, "Multi-resolution open-top light-sheet microscopy to enable efficient 3D pathology workflows," *Biomed. Opt. Express*, 11 (11), 6605 (2020).

[43] M. Weber and J. Huisken, "Light sheet microscopy for real-time developmental biology," *Curr. Opin. Genet. Dev.*, 21, 566–572 (2011).

[44] P. J. Keller, A. D. Schmidt, J. Wittbrodt, and E. H. K. Stelzer, "Digital scanned laser light-sheet fluorescence microscopy (DSLM) of zebrafish and drosophila embryonic development," *Cold Spring Harb. Protoc.*, 1235–1243, (2011).

[45] K. Chung *et al.*, "Structural and molecular interrogation of intact biological systems," *Nature*, 497, 332–337 (2013).

[46] E. A. Susaki, K. Tainaka, D. Perrin, H. Yukinaga, A. Kuno, and H. R. Ueda, "Advanced CUBIC protocols for whole-brain and whole-body clearing and imaging," *Nat. Protoc.*, 10 (11), 1709–1727 (2015).

[47] N. Renier, Z. Wu, D. J. Simon, J. Yang, P. Ariel, and M. Tessier-Lavigne, "IDISCO: A simple, rapid method to immunolabel large tissue samples for volume imaging," *Cell*, 159 (4), 896–910 (2014).

[48] B. Balázs, J. Deschamps, M. Albert, J. Ries, and L. Hufnagel, "A real-time compression library for microscopy images," *bioRxiv* (2017).

[49] D. Hörl *et al.*, "BigStitcher: reconstructing high-resolution image datasets of cleared and expanded samples," *Nat. Methods*, 16, 870–874 (2019).

[50] M. Zhou, Jiambo Li, Liang Cheng, Lars Egevad, and F.-M. Deng, "Diagnosis of 'poorly formed glands' Gleason pattern 4 prostatic adenocarcinoma on needle biopsy," *Am. J. Surg. Pathol.*, 39 (10), 1331–1339 (2015).

[51] O. Hassan and A. Matoso, "Clinical significance of subtypes of Gleason pattern 4 prostate

cancer," *Transl. Androl. Urol.*, 7, S477–S483 (2018).

[52] N. P. Reder, A. K. Glaser, E. F. McCarty, Y. Chen, L. D. True, and J. T. C. Liu, "Open-top light-sheet microscopy image atlas of prostate core needle biopsies," *Arch. Pathol. Lab. Med.*, 143, (9), 1069–1075, (2019).

[53] A. Stankov, J. E. Bargallo-Rocha, A. Ñ.-S. Silvio, M. T. Ramirez, K. Stankova-Ninova, and A. Meneses-Garcia, "Prognostic Factors and Recurrence in Breast Cancer: Experience at the National Cancer Institute of Mexico," *ISRN Oncol.*, 2012, 1–7 (2012).

[54] G. N. Hortobagyi *et al.*, *AJCC Cancer Staging Manual*, vol. 48, no. Eighth Edition. 2017.

[55] G. Cserni, "Complete sectioning of axillary sentinel nodes in patients with breast cancer. Analysis of two different step sectioning and immunohistochemistry protocols in 246 patients," *J. Clin. Pathol.*, 55 (12), 926–931 (2002).

[56] E. P. Mamounas *et al.*, "Effect of serial sectioning and immunohistochemistry (IHC) on sentinel lymph nodes (SLNs) on the false-negative rate (FNR) of SLN biopsy (SLNB): Results from NSABP B-32," *J. Clin. Oncol.*, 29 (27), 86–86 (2011).

[57] L. A. Barner *et al.*, "Multiresolution nondestructive 3D pathology of whole lymph nodes for breast cancer staging," *J. Biomed. Opt.*, 27, 1–13 (2022).

[58] E. A. Susaki *et al.*, "Versatile whole-organ/body staining and imaging based on electrolyte-gel properties of biological tissues," *Nat. Commun.*, 11 (1), 1982 (2020).

[59] C. Mao *et al.*, "Feature-rich covalent stains for super-resolution and cleared tissue fluorescence microscopy," *Sci. Adv.*, 6 (22), 1–10 (2020).

[60] E. Murray *et al.*, "Simple, Scalable Proteomic Imaging for High-Dimensional Profiling of Intact Systems," *Cell*, 163 (6), 1500–1514 (2015).

[61] K. N. Elfer *et al.*, "DRAQ5 and eosin ('D&E') as an analog to hematoxylin and eosin for rapid fluorescence histology of fresh tissues," *PLoS One*, 11 (10), 1–18 (2016).

[62] K. Matsumoto *et al.*, "Advanced CUBIC tissue clearing for whole-organ cell profiling," *Nat. Protoc.*, 14 (12), 3506–3537 (2019).

[63] A. K. Glaser *et al.*, "A hybrid open-top light-sheet microscope for multi-scale imaging of cleared tissues," *bioRxiv* (2021).

[64] S. Nojima *et al.*, "CUBIC pathology: Three-dimensional imaging for pathological diagnosis," *Sci. Rep.*, 7 (1), 1–14 (2017).

[65] D. S. Richardson and J. W. Lichtman, "Clarifying Tissue Clearing," *Cell*, 162 (2), 246–

256 (2015).

[66] J. Schindelin *et al.*, “Fiji: An open-source platform for biological-image analysis,” *Nat. Methods*, 9 (7), 676–682 (2012).

[67] S. Samphao, J. M. Eremin, M. El-Sheemy, and O. Eremin, “Management of the axilla in women with breast cancer: Current clinical practice and a new selective targeted approach,” *Ann. Surg. Oncol.*, 15 (5), 1282–1296 (2008).

[68] B. C. H. van der Wal, R. M. J. M. Butzelaar, S. van der Meij, and M. A. Boermeester, “Axillary lymph node ratio and total number of removed lymph nodes: Predictors of survival in stage I and II breast cancer,” *Eur. J. Surg. Oncol.*, 28 (5), 481–489 (2002).

[69] S. Y. Kim *et al.*, “Stochastic electrotransport selectively enhances the transport of highly electromobile molecules,” *Proc. Natl. Acad. Sci. U. S. A.*, 112 (46, (2015).

[70] B. Qumseya *et al.*, “ASGE guideline on screening and surveillance of Barrett’s esophagus,” *Gastrointest. Endosc.*, 90 (3), 335–359 (2019).

[71] M. J. Whitson and G. W. Falk, “Predictors of Progression to High-Grade Dysplasia or Adenocarcinoma in Barrett’s Esophagus,” *Gastroenterol. Clin. North Am.*, 44 (2), 299–315 (2015).

[72] F. Hvid-Jensen, L. Pedersen, A. M. Drewes, H. T. Sorensen, and P. Funch-Jensen, “Incidence of adenocarcinoma among patients with Barrett’s esophagus,” *N. Engl. J. Med.*, 365 (15), 687–696 (2011).

[73] S. J. Spechler, “Barrett esophagus and risk of esophageal cancer: A clinical review,” *JAMA - J. Am. Med. Assoc.*, 310 (6), 627–636 (2013).

[74] L. Lekakos, N. P. Karidis, D. Dimitroulis, C. Tsigris, G. Kouraklis, and N. Nikiteas, “Barrett’s esophagus with high-grade dysplasia: Focus on current treatment options,” *World J. Gastroenterol.*, 17 (37), 4174–4183 (2011).

[75] M. F. Berry, “Esophageal cancer: Staging system and guidelines for staging and treatment,” *J. Thorac. Dis.*, 6, 289–297 (2014).

[76] D. A. Leffler *et al.*, “The incidence and cost of unexpected hospital use after scheduled outpatient endoscopy,” *Arch. Intern. Med.*, 170 (19), 1752–1757 (2010).

[77] N. Otsu, “A threshold selection method from gray-level histograms,” *IEEE Trans. Syst. Man. Cybern.*, 1, 62–66 (1979).

[78] K. He, X. Zhang, S. Ren, and J. Sun, “Deep residual learning for image recognition,”

Proc. IEEE Comput. Soc. Conf. Comput. Vis. Pattern Recognit., 770–778 (2016).

[79] D. Wang, A. Khosla, R. Gargeya, H. Irshad, and A. H. Beck, "Deep Learning for Identifying Metastatic Breast Cancer," *arXiv*, (2016).

[80] L. Pantanowitz *et al.*, "Validating whole slide imaging for diagnostic purposes in pathology: guideline from the College of American Pathologists Pathology and Laboratory Quality Center," *Arch. Pathol. Lab. Med.*, 137 (12), 1710–1722 (2013).

[81] W. Xie *et al.*, "Prostate Cancer Risk Stratification via Nondestructive 3D Pathology with Deep Learning–Assisted Gland Analysis," *Cancer Res.*, 82 (2), 334–345, (2022).

[82] L. A. Barner *et al.*, "Multiresolution nondestructive 3D pathology of whole lymph nodes for breast cancer staging," *J. Biomed. Opt.*, 27 (3), 1–13 (2022).